Reducing slipstream velocities around high-speed trains through retractable stationary surfaces

Jordan Ashley Dunlop *, Mark Christopher Thompson

Fluids Laboratory for Aeronautical and Industrial Research, Department of Mechanical and Aerospace Engineering, Monash University, PO Box 31, Clayton, 3800, Australia

ARTICLE INFO

ABSTRACT

The slipstream wake structures generated by the passing of high-speed rail vehicles represents a hazard to passengers and workers in close proximity, and as such, maximum allowable slipstream velocities are prescribed in regulations. In this article, the possibility of reducing peak slipstream velocities using retractable or foldable local surface modifications on a generic high-speed train is assessed using Improved Delayed Detached Eddy Simulation (IDDES) modelling. It is demonstrated that the danger imposed by the slipstream wake structures, as measured by the induced velocities recorded at a pair of parallel test lines, as dictated in the standards, could be reduced by designs employing each of three methods examined. The most dramatic reductions were generated by large fins at the train rear, which redirected the time-mean trailing vortex structures to one side of the vehicle. However, the most feasible control method for symmetrical slipstream reduction consisted of placing small rectangular plates perpendicular to the flow near the nose section of the train. The induced disruption to the flow was observed to increase wake turbulence in a region above the train, which appeared to interfere with the formation of the trailing vortex structures and reduce the intensity of the cross-stream oscillation.

© 2023 Elsevier Masson SAS. All rights reserved.

1. Introduction

Over the last 50 years advances in the understanding of train aerodynamics has allowed for a dramatic increase in the velocities at which rail vehicles can travel. A high-speed train is generally regarded as a rail vehicle that spends a significant portion of its travel time at velocities over 200 km/h, although speeds can be significantly greater than this.

At such extreme velocities, aerodynamics is not only key in minimising drag but also in managing the generation of large slipstream structures that arise in the wake of these vehicles as they travel. Slipstream flows are defined (e.g. see [1]) as "the air flow induced by the train's movement as experienced by a stationary observer". High induced velocities can extend to a sufficient spanwise distance from the tracks so as to pose a safety risk to people located in close proximity of passing trains, most commonly commuters waiting at stations and track-side workers. This is addressed in [2], where it is suggested that gust speeds as low as 15 m/s could be sufficient to cause people to "stumble or be displaced". The complex instantaneous wake structure responsible for the peak slipstream velocities is shown in Fig. 1(b) together with the 50:3:4 (length:width:height) reduced aspect-ratio model of a *Deutsche Bahn Inter-City Express 3*,

or ICE-3, high-speed train which served as the baseline for this investigation (Fig. 1(a)).

As such, there are restrictions in place to limit the peak slipstream velocities tolerated near passing trains. The European Railway Agency (ERA) enforces a set of regulations known as the *Technical Specifications for Interoperability* or TSI, which specify the limits for the allowable slipstream velocities. Formally, the slipstream velocity measure used in the regulations requires a sample of more than 20 passes of the test vehicle, from which measurements of the maximum slipstream velocities at a point 3 m from the centre of the track and 1.2 m above the platform are recorded. From this sample, the mean value plus two standard deviations is used to generate a measure of the (maximum) slipstream velocity. The inclusion of this regulation indicates that reducing the magnitude of slipstream velocities experienced by commuters as a high-speed train passes is an issue of concern for both designers and operators. The slipstream behaviour of high-speed trains is hence an area of great interest in vehicular aerodynamics. Investigating the behaviour of these flows is commonly performed through three separate but interlinked methodologies: full-scale field testing, reduced-scale wind-tunnel testing and computational fluid dynamics (CFD) simulations.

Studies based on full-scale field testing of high-speed trains are limited, due to the costs of obtaining an operational vehicle for the significant period of time required so as to generate a sufficiently large data set. However, when they are performed,

---

* Corresponding author.
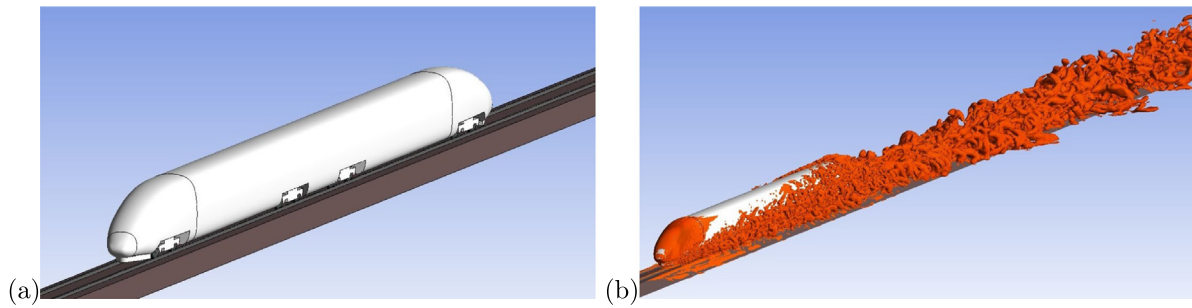   *E-mail address:* jordan.dunlop@monash.edu (J.A. Dunlop).

Fig. 1. (a) ICE-3 high-speed train model used for the baseline test case. (b) Isosurface of instantaneous Q-criterion of 1000 s^{-2} demonstrating the formation of highly turbulent wake structures behind ICE-3 high-speed train model.

these studies are vital in obtaining practical results without the constraints and limitations that arise from the approximations other methods employ to attempt to replicate these real-life flows. The studies of Baker et al. [3,4] investigated and cataloged the slipstream behaviour of a large variety of trains, including the ICE-3 high-speed train, the model on which this study is based. One key result relevant to this investigation is the set of locations of the largest ensemble-average slipstream velocities for the high-speed trains tested. For a range of heights above the platform, two key velocity spikes were observed to occur, one at the passing of the nose of the train and a larger peak a small distance downstream of the tail of the train. These results provide a basis for the expected slipstream velocity distributions obtained from this study. Full-scale testing can also serve as a means of validating a computational or experimental model, such as in [5], where a numerical model investigating train overturning is validated through testing on a full-scale vehicle.

Reduced-scale wind tunnel testing is a more commonly applied method for examining slipstream behaviour, allowing significantly more freedom to test a range of variables such as crosswinds, cornering trains and design alterations. Indeed, this study follows on from the extensive wind-tunnel testing programmes conducted by Monash University on scale-models of the ICE-2 and ICE-3 high-speed trains. Early work, such as Bell et al. [1,6,7] focused on analysing the characteristics of high-speed train wake profiles in considerable depth, and examined the spanwise oscillation of the trailing counter-rotating vortex pair as a leading cause of large slipstream disturbances in the wake. A later study, Bell et al. [8], explored large-scale redesigns of the tail geometry as a means of slipstream control. It was observed that by increasing the angle at which the tail diverged from the train body, so as to generate a sharper edge, slipstream velocities could be potentially reduced, but at the cost of increased pressure drag. This identified that the most streamlined designs did not necessarily result in the smallest slipstream velocities, and suggested that there may be a better compromise between reducing these measures and the drag force experienced by the train.

A common limitation of reduced-scale wind-tunnel testing is that generally experiments are conducted with a stationary ground. As such, differences can arise near the ground due to boundary-layer formation that would not be present in practice, where the train is moving relative to the ground. One method of addressing this is to conduct experiments by passing a scale model along a section of track and recording velocities at the trackside locations, as performed in [9]. Unfortunately such testing is considerably more time consuming and generally conducted at lower Reynolds numbers, given the restrictions in the size of the model and test velocities possible. An approach implemented in [10] to address this first issue was to develop a rotating rail rig, so that a train model could traverse a circular path, so as to quickly generate a large data set. This approach

however, further exaggerates the Reynolds number issue, as the model is reduced to a 1/50th scale, and the test velocity to 22 m/s, well below velocities achievable in standard wind-tunnel testing, or even straight-line moving model experiments such as Bell et al. [9] (32 m/s). Additionally as the track is circular, all measurements are recorded with the model in a continuous turning motion, leading to a question of how well the results apply to trains travelling in a straight line.

Computational fluid dynamics (CFD) has become increasingly important as a design and analysis tool over the last few decades. Simulating high Reynolds number flows accurately enough to provide useful insight requires significant amounts of computing power and processing time, but developments in supercomputing and parallel chip technologies have led to CFD joining reduced-scale wind-tunnel testing as a cost-effective method of analysing complex flows. Early high-speed train research by Hemida and Baker [11] applied Large-Eddy Simulation (LES) turbulence modelling techniques to study slipstream behaviour around a simplified ICE-2 train geometry. When compared to Baker et al. [3,4], track-side time-averaged slipstream velocity measurements indicated a similar dual peak profile, at the nose and shortly after the tail of the train, but with a considerably more uniform velocity profile observed at downstream distances corresponding to the body of the train. The advantages of CFD as an experimental method is demonstrated by the ability of Hemida and Baker [11] to monitor slipstream conditions at a large range of spanwise locations, illustrating the variation in the streamwise location of the peak slipstream velocities at different spanwise separations. CFD is also a very useful tool for generating detailed wake profiles, such as those seen in [12], where Proper Orthogonal Decomposition (POD) and Dynamic Mode Decomposition (DMD) are used to visualise the time-mean counter-rotating vortex cores that dominate high-speed train wakes.

A further benefit of computational modelling is the greater ease with which design alterations can be applied and subsequently tested. A similar approach of using CFD to investigate the effect of structural changes is seen in [13], where the nose length of a high-speed train model is altered and Improved Delayed Detached Eddy Simulations (IDDES) are employed to demonstrate that the slipstream velocities at the TSI specified positions can be reduced by extending the length of the nose, with 15 and 22% reductions recorded by increasing the nose length from 5 m to 7.5 m and 10 m respectively. A similar modification of the nose region of a high-speed train is explored in [14], however with a greater focus on drag reduction. A numerical optimisation of the nose region was shown to be capable of reducing the total aerodynamic drag by 2%. Further recent studies that also utilised IDDES modelling of high-speed trains are [15], which illustrated that increasing the size of bogie fairings can produce up to 16% reductions in the maximum slipstream velocities, and [16], which examined a range of ground clearances for an ICE-3 high-speed
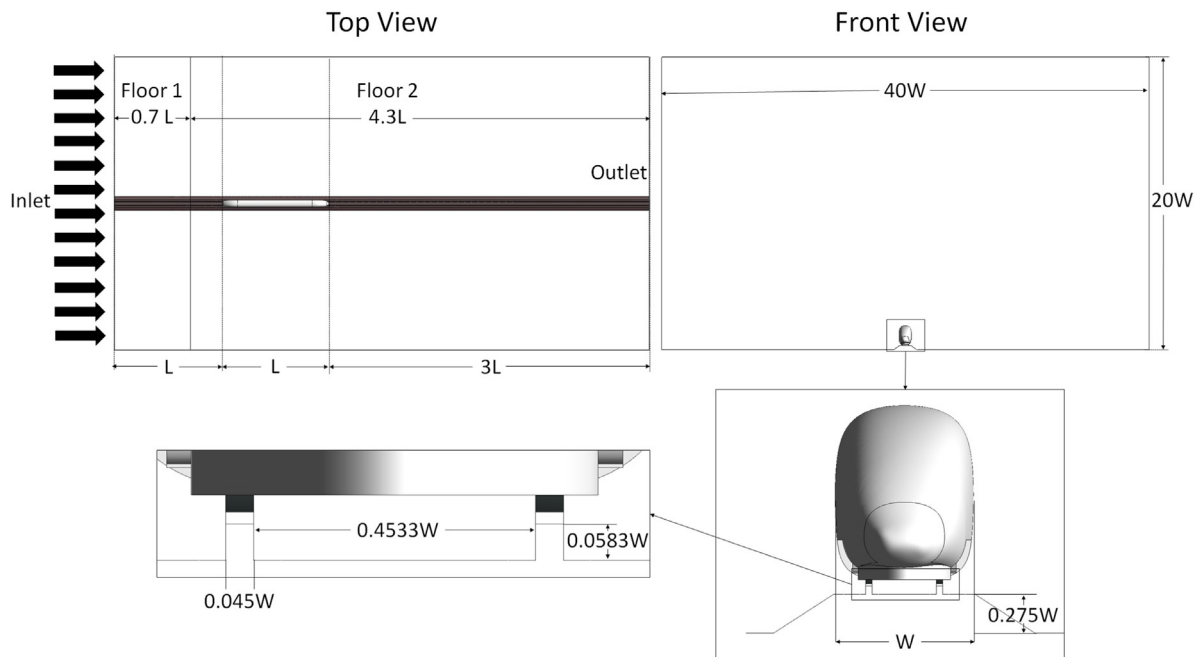
Fig. 2. Dimensions and layout of the computational model.

train and the effect of these changes on the height and spanwise separation of the counter-rotating vortex core structures that are key to large slipstream disruptions.

The key difficulty that arises from using CFD is verifying that simulation predictions are replicating real-world behaviour. As such, studies such as Wang et al. [17] are crucial in establishing model requirements that produce a good match with results obtained from experimental studies. In particular, Wang et al. [17] compared simulation predictions with reduced-scale wind-tunnel tests [1,6,7], examining the spatial and temporal resolution requirements and the effect of different turbulence models to accurately replicate the slipstream flow behaviour around an ICE-3 train model. Comparisons with experiments indicated that the IDDES model produced the most robust and reliable predictions.

This study builds on the validated methodology of Wang et al. [17,18] to investigate whether applying passive structural elements to the surface of an ICE-3 train model can feasibly reduce wake slipstream velocities. The rationale for the choices of add-on structural elements is either to attempt to redirect the time-mean counter-rotating vortex cores, previously observed to be key to large slipstream peaks, away from the passenger locations, or through attempting to disrupt or weaken these problematic flow structures as they form. As high-speed trains are always designed to have the minimal drag practically achievable, it is a key consideration that the drag rise induced from the addition of these surfaces is monitored, and that the potential for the structural elements to be retracted or folded when not required be considered. Some of the designs tested are potentially larger than could practically be designed to retract cleanly into the body of the train and thus are considered as a proof-of-concept designs, to determine if there is any potential for a smaller, more retractable design to be implemented. Of course, it is noted that aircraft use retractable surfaces in a similar manner to significantly increase lift during takeoff and landing.

2. Methodology

This study is comprised of two stages: a preliminary series of tests, where a large number of potential designs were explored, and a second series of tests, where more refined meshes and increased simulation times were used to examine the most promising designs from stage one. The setup described below was used for the preliminary tests. Subsequently, a description of modifications applied to second set of tests is provided.

2.1. Computational modelling parameters

2.1.1. Computational domain

The high-speed train geometry used in this study is the same as employed in [17]: a simplified single-carriage replication of a *Deutsche Bahn Inter-City Express 3* or ICE-3 high-speed train with a length–width–height ratio of approximately 50:3:4, compared to a general configuration of 200:3:4. This length reduction is due to the considerable computational cost of using a longer computational model, with an estimated reduction in computational run-time of a factor of 4 and the required memory a factor of 2.5. The train is placed on a single-track ballast and rail ground configuration. This layout is shown in Fig. 2.

The ground surface is flat and no crosswind is present. The inlet of the domain is one-train length forward of the nose of the model and the outlet is positioned three-train lengths rear of the tail of the train to allow for slipstream structures to develop and persist sufficiently downstream. All designs are tested subject to a *moving floor*, therefore, the surfaces that constitute the train model remain stationary, while the flow moves past the train at the specified inlet velocity with matching linear motion of the ground, ballast and rail surfaces. For verification of the baseline case, a *stationary floor* model was also explored for comparison with wind-tunnel experiments. In that case, the floor for the first 0.7 train lengths from the inlet (Floor 1, see Fig. 2) was defined as a zero-shear wall, while the remaining floor (Floor 2, see Fig. 2) was defined as a no-slip wall. The intention of this was to approximate the splitter plate configuration employed in wind-tunnel testing [1]. A zero pressure outlet was used with zero-gradient velocity components. The width and height of the domain are 40 and 20 train widths respectively, yielding a blockage ratio of 0.17%. In the following, the width of the train is used as the reference length (L_{Ref}).

Table 1

Comparison of magnitude and downstream location of maximum ensemble slipstream velocities, magnitude and downstream location of maximum standard deviation of ensemble slipstream velocities and drag coefficient values for 0.025 T_{ref} and 0.0025 T_{ref} timesteps when utilising the fine mesh and IDDES turbulence model from [17].

Timestep	$\bar{U}$ max	$\bar{U}$ location (x/H)	σ max	σ location (x/H)	C_D
0.025 T_{ref}	0.119	6.61	0.078	5.61	0.274
0.0025 T_{ref}	0.120	6.56	0.079	5.61	0.273

Table 2

Mesh category specifications.

Mesh subdivision	Element size (L_{Ref})	Inflation layer growth rate
Coarse	1/30	1.35
Fine	2/75	1.30
Finest	1/60	1.22

Table 3

Dimensions and element size of the four refinement zones (all distances are standardised by L_{Ref}).

Body of influence	Origin (x)	Length (x)	Width (y)	Height (z)	Element size
Under-body	2/3	19	2/3	2/3	1/120
Train body	1 2/3	25	5 1/3	2	1/15
Direct wake	6 2/3	75.53	2 2/3	1.17	1/15
Far-field wake	6 2/3	75.53	5 1/3	2 2/3	4/15

Table 4

Mesh resolution study - 5 degree large fins.

Drag coefficient	Coarse	Finest	Double
C_D	0.2780	0.2787	0.2790
ΔC_D (%)	−0.35	−0.11	–
POD - Slipstream Velocity			
Mean (%)	−0.08	−0.01	–
Fluctuating (%)	−7.42	1.13	–
Mode 1 (%)	−5.32	−1.19	–

2.1.2. Solver settings

As in [17,18], ANSYS FLUENT was employed for all simulations. Testing was conducted at a Reynolds number of 720,000 (where $Re = \frac{\rho U L}{\mu}$), corresponding to an inlet velocity (U_{Inlet}) of 35 m/s for the 1/10th-scale model, matching the scale-model wind-tunnel studies of Bell et al. [1,6,7]. An inlet turbulent intensity of 1% was applied, which is typical of wind-tunnel facilities. Whilst [17] examined a range of turbulence models, this study only employed the IDDES model incorporating the Shear-Stress Transport $k-\omega$ RANS model for near-wall zones, noting predictions of Wang et al. [17] indicated this model produced a better fit to the experimental data over a range of alternatives. The selection of the timestep was also based upon the results of Wang et al. [17], where minimal variation was observed in slipstream and drag predictions when the timestep was varied by an order of magnitude between 0.025 and 0.0025 T_{ref}, as shown in Table 1.

As such, a timestep of 0.033 T_{ref}, where $T_{ref} = L_{Ref}/U_{Inlet}$, was selected. Note that this timestep size is equivalent to the 0.025 T_{ref} value presented in [17], as that study used the height of the vehicle, rather than the width, as the reference length, and these values follow a 4:3 ratio. The sample size employed for the primary test series was to allow a settling period of 66.7 T_{ref} and then a sampling period of 200 T_{ref}, once again on the basis that this sampling period employed by Wang et al. [17] was found to provide reasonably converged flow statistics.

2.1.3. Meshing parameters

The construction of the computational mesh follows that of Wang et al. [17], and was generated by subdivision of surfaces into three categories: termed *coarse*, *fine* and *finest* resolutions. Surfaces were categorised on the basis of the expected degree of flow variation at the location, as well as the perceived importance of the region to the wake formation. The mesh was generated using ANSYS Meshing, employing the *Cartesian Cut-Cell* assembly approach. Each mesh subdivision was defined by a specified element size and the allowable growth rate of inflation layers; thin elements located on surfaces to capture flows within the boundary layer. These settings are shown in Table 2. All inflation layers were generated using the *smooth transition* option, and had a maximum of 10 layers.

Similar inflation layers were also present on the floor and ballast surfaces, utilising a growth rate of 1.30, where transient flow interactions with the surface were expected, even though a boundary layer profile would not develop for the cases where a moving floor model was employed. As the mesh extended further away from the surface of the model, the element sizing was further restricted by a set of four refinement zones or bodies of influence. All four zones consisted of rectangular prisms, far longer

in the streamwise direction than in the spanwise or vertical directions. The element sizings of each region, were again based on those used in [17] to generate the fine mesh. The dimensions of each zone are summarised in Table 3, along with the specified element size. Note that the origin is the distance upstream of the nose of the train model at which the refinement zone commences. All four zones are symmetrical about the spanwise (y) centre-plane and have their base on the floor of the domain.

In comparison to the baseline mesh, the new design cases were only altered by assigning the added surfaces into a mesh subdivision. To determine which subdivision was adequately resolved, a mesh resolution study was conducted for the test case of the inwards deflected fins at a 5° deflection angle. This case was examined by generating meshes in which the fins were placed into the *coarse* and *finest* subdivisions, as well as a new set of specifications, with the element size halved again from the *finest* to 1/120 L_{Ref} and the inflation layer growth rate further reduced to 1.10. This subdivision will be referred to as *double*. This mesh resolution study consisted of drag coefficient analysis and a flow energy comparison, utilising Proper Orthogonal Decomposition (POD) to examine the energy of the slipstream velocity in a horizontal plane surrounding the fins, both seen in Table 4.

It was observed that the drag differential was less than 0.4% for all three subdivisions, with the value for the *finest* subdivision only varying from that of the *double* by 0.11%, while the POD results also indicated significantly greater improvement when moving from the coarse to finest subdivision than from finest to double. Given the highly turbulent nature of the flow this was deemed to be within the expected uncertainty range, and an indication that the mesh was adequately resolved when using the *finest* subdivision for the primary test series. A variety of mesh cross-sections, demonstrating these refinements, can be seen in Fig. 3. The result of these settings was a model that required approximately 27,500 computer hours to simulate the full 266.67 T_{Ref} (66.67 T_{Ref} settling period, 200 T_{Ref} sampling period) required for each new design.

2.2. Verification of model

To verify the adequacy of the model detailed above, a number of different predictions were compared with published data from past research. Firstly, a one-second moving-average slipstream measure at the *trackside height* (a full-scale 0.2 m above the platform) was generated using combination of the 0.033 T_{ref} timestep, fine mesh and IDDES turbulence model, as this result
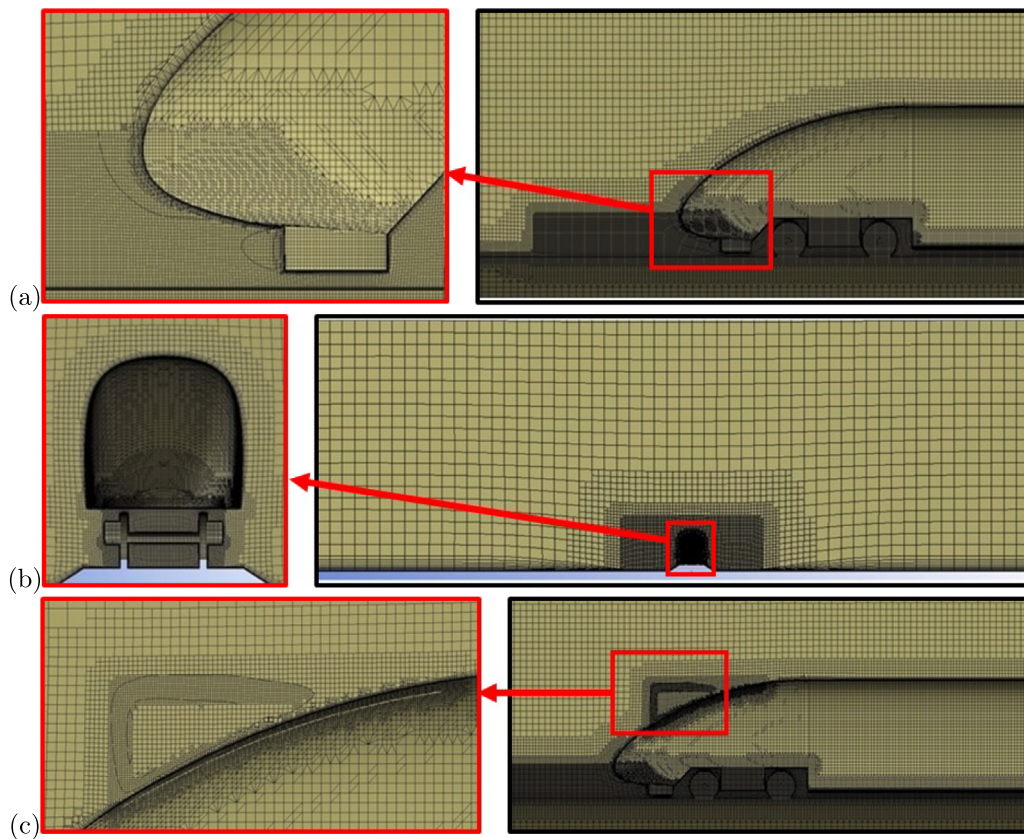
Fig. 3. Cross-sections at the (a) spanwise and (b) streamwise locations of the model's front axle illustrating the computational mesh and highlighting regions of significant mesh refinement for the baseline model. (c) Cross-section at the spanwise location of 2° deflected large fin, showing regions of mesh refinement around an added control device.

was not presented in [17]. This combination returned a value of 0.1625, 2% off the value of 0.159 presented for the fine mesh, IDDES turbulence model and 0.0025 T_{ref} timestep combination in [17], which had in turn been shown to match well wind-tunnel measurements of Bell et al. [1], which also returned a measure of 0.159. This provided confidence that the larger timestep would not compromise the validity of predictions.

Given the locations of the proposed control surfaces were along the roof of the train, comparison was also made to the roof boundary-layer profile shown in the moving-model tests of Bell et al. [9], by examining the streamwise velocity at the 5 specified heights above the roof.

Fig. 4(a) illustrates that despite a reduced aspect ratio (L/H = 12.5 vs 16), increased Reynolds number (720,000 vs. 330,000) and lack of inter-carriage gaps, the overall profile shows good reproduction of the trends for each height. This is seen particularly in the similarity in magnitude and location of peak velocity deficits recorded at each test height. The most significant variation stems from the inability of experimental moving-model tests to record velocity rises, as Fig. 4(a) indicates that near the nose the velocity increases by up to 10% of U_{Inlet}. This is further seen in Fig. 4(b), as the full-scale 10 m location records velocity rises at the 3 probes furthest from the surface, indicative of accelerated flow over the nose of the train. Overall these results provide confidence in the model to predict the conditions in the roof boundary layer accurately, and thus illustrates that the lack of inter-carriage gaps is unlikely to affect the validity of the results.

The wake structures were also compared to those recorded experimentally in [7], through the decay of the top 100 POD modes of the total pressure at planes 1 to 6 train heights downstream. The variation that occurs from modifying the ground conditions

is also shown, with a different distribution emerging when the moving floor model is applied, as seen in Fig. 5(b).

Fig. 5(a) shows a good replication of the decay in mode 1 energy as the flow moves further downstream, as well as the relative energy levels of the higher order modes. Fig. 5(b) illustrates that a moving floor significantly decreases the relative energy in the near wake of the dominant mode as well as reducing the decay in energy of this mode as it moves further downstream.

Finally, the frequency response of the dominant mode of the slipstream velocity was compared to values obtained in prior studies, focusing on the peak Strouhal number. Bell et al. [1] estimated a Strouhal number of 0.18 for the dominant mode in the wake of an ICE-2 high-speed train, whilst values of 0.11 from [19], 0.14 from [20] and 0.13 from [12] have been estimated for this mode from varying high-speed train models. In this study, when utilising a moving floor model, a mean Strouhal number of 0.178 was obtained from multiple test planes in the wake for the unmodified baseline train model, with this value increasing only marginally to 0.180 when the alternative, stationary floor model was employed. Whilst this frequency response is not significantly affected by the change in ground condition, local shedding frequencies are, as shown in [18], where the wake shedding frequency at the point [1H, −0.4W, 0.2H] is observed to increase significantly when switching from a stationary to moving floor. This observation was replicated in this study, with the *local* Strouhal number increasing from 0.33 to 0.65 at the same location. As such, these results match well with the most closely linked prior research of Bell et al. [1] and Wang et al. [18], and indicate that while the local frequency response may be affected by the ground condition, the key oscillation of the highest order mode is not.
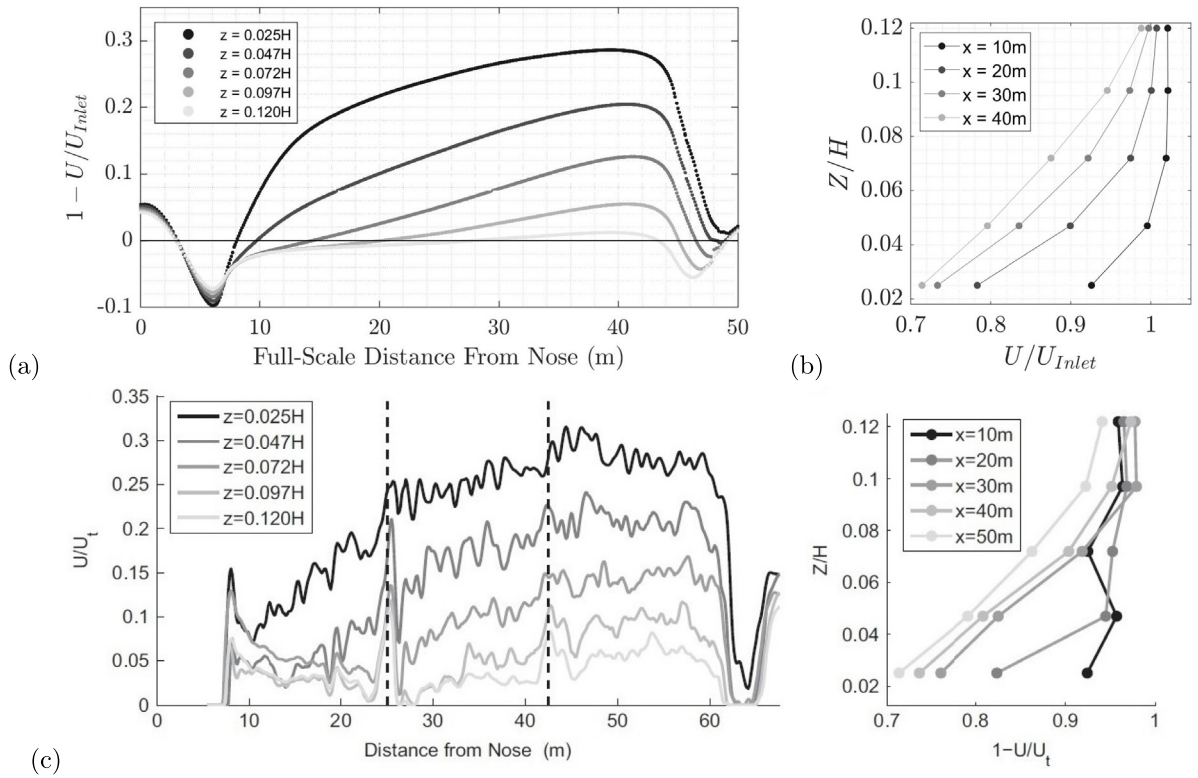
Fig. 4. (a) Ensemble average streamwise velocity deficit at 5 non-dimensionalised heights above the roof. (b) Roof boundary layer profile at multiple full-scale distances downstream of nose. (c) Figures from [9] for comparison.
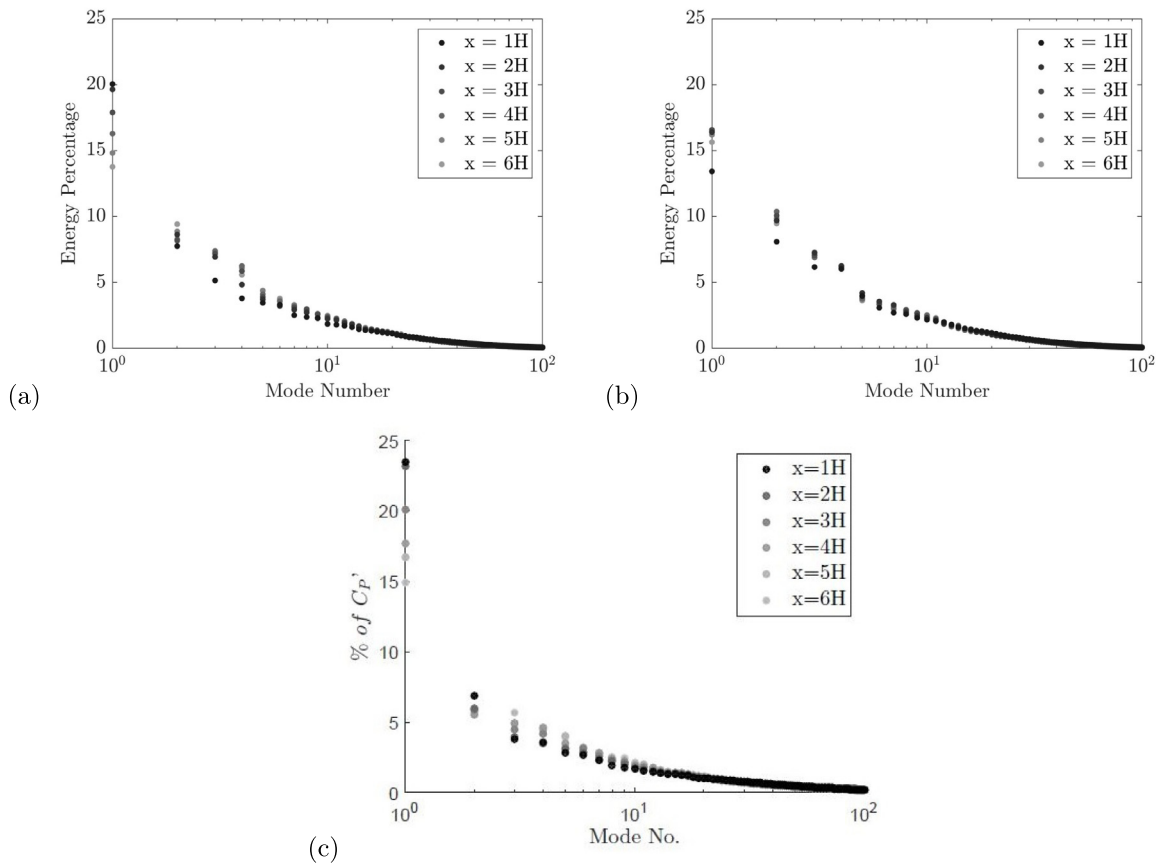

Fig. 5. Energy contributions of top 100 fluctuating POD modes of total pressure at planes 1 to 6 train heights (H) downstream, utilising a (a) stationary and (b) moving floor model. (c) Figure from [7] for comparison.
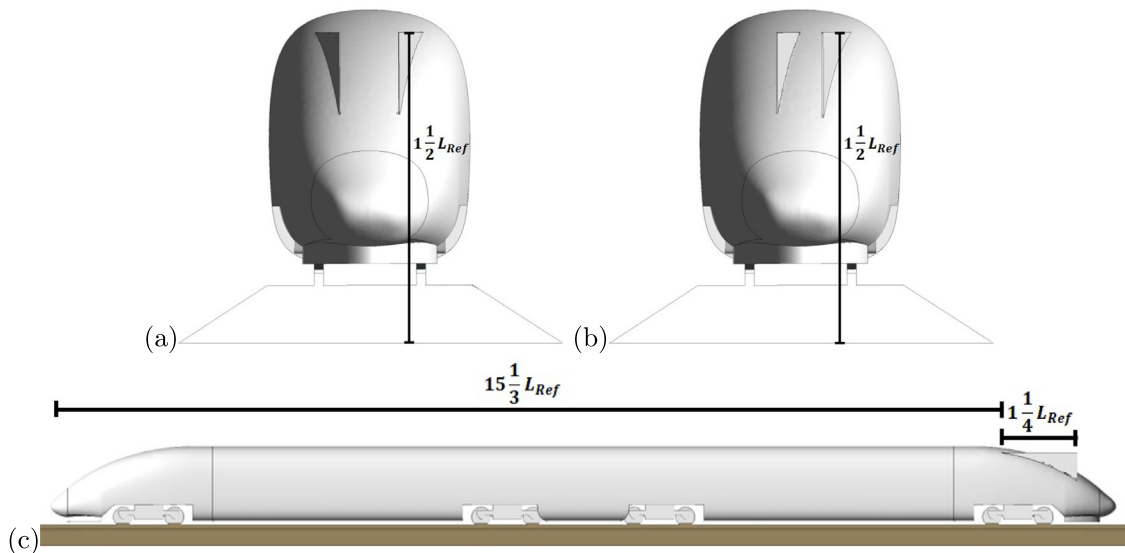
Fig. 6. Rear view of (a) inwards deflected fins at 6 degrees deflection and (b) parallel fins at 7 degrees deflection. (c) Side view of the fins *before* any rotation is applied.

These comparisons to past work thus provides further confidence in the validity of the model, as well as highlighting some of the differences that employing a more realistic moving floor model has on the wake behaviour.

2.3. Flow alteration devices

The three categories of flow alteration devices are discussed below, highlighting the size, position and desired effects.

2.3.1. Inwards deflected fins

The work of Muld [12] and Bell et al. [7] has identified that a dominant feature of the time-mean wake topology of high-speed trains is a trailing counter-rotating vortex pair generated at the tail of the train. Moreover, these trailing vortices oscillate across the wake and large instantaneous excursions occur, causing high velocity fluid to deviate a considerable cross-stream distance from the train centreline. The first set of designs tested were intended to determine whether these vortex cores could be redirected inwards, towards the centreplane, as they were forming. This flow redirection was generated through the addition of fins, with converging angles of between 2 and 7°. It was hypothesised that this flow redirection may cause the vortex pair to require a larger downstream distance for significant excursions to extend out to the test locations, by which time a significant portion of the energy of these structures will have dissipated through turbulent diffusion.

The design used was a pair of simple, large triangular fins, to at least act as a proof-of-concept that the flow could be significantly altered by a control surface placed in this location. The fins were positioned on the downwards slope of the rear of the train geometry, with a flat upper surface emerging smoothly from the train geometry at a distance 15.33 L_{Ref} downstream from the nose of the train, a steady height of 1.5 L_{Ref} above the floor and extending 1.25 L_{Ref} downstream (when no deflection angle was applied), until ceasing at a right angle down to the surface of the initial geometry (see Fig. 6(c)).

The fins were 1/120 L_{Ref} thick and had a base spanwise displacement of 1/4 L_{Ref} from the centre-plane, placing the pair of fins 1/2 L_{Ref} apart *before* the deflection was applied around centre-point.

2.3.2. Parallel fins

An variation of this large fins design was to re-position and re-orient one of the fins so that the deflection was in the same direction for both, with the aim of redirecting the vortex cores to a single side of the train. It was expected that this solution would only offer an advantage in the circumstances in which one side of the platform was to be occupied, as it was expected that the side to which the vortex pairs were redirected would experience an increase in induced slipstream velocities. The same fin from the inwards deflected fin designs was used as the basis of this design, and thus the same size and placement specifications apply at 0° deflection angle. The fins were separated so as to be equidistant from the centre-plane at their trailing edges, based on the positioning of the fin which had not had its angle reversed. This meant that the two fins would emerge from the geometry at different distances from the centre-plane and, given the curvature of the train geometry, differing downstream distances. The same range of deflection angles (2–7°) were examined. An example of the deflection angle of 7° is shown in Fig. 6(b).

Due to the lack of mirror symmetry for this design, when determining the slipstream velocities at the test position, it was necessary to examine the lines on either side of the train independently. In the following discussions, the test positions on the side to which both fins are angled towards (positive y direction) will be referred to as the *danger side*, whilst the side from which the fins are angled away from will be referred to as the *passenger side*.

2.3.3. Blocker plates

The final design proposed for reducing slipstream velocities was to place flat, rectangular plates perpendicular to the inlet flow at varying streamwise locations along the length of the train's roof. The plates were located in spanwise areas corresponding to the regions at which, at the tail of the train, vortex pair formation was observed to occur on the baseline model. The intention of the blocker plates was to disrupt the flow that leads to this formation, rather than redirecting it in a spanwise direction, as was the intention of previous, fin based designs. The default width of the plates was 1/6 L_{Ref}, with each plate positioned so the gap between the centre-plane and the inner edge of the plate was also 1/6 L_{Ref}. The plates height was defined so that the tip was at a height of 5/3 L_{Ref} above the ground,
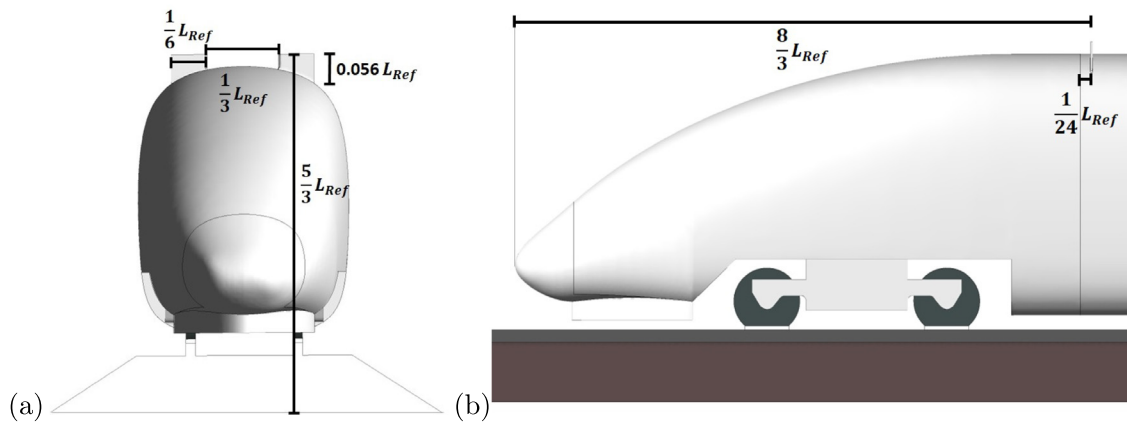
Fig. 7. (a) Front and (b) side view of standard sized blocker plates at the forward position.

meaning that the plates extended to a maximum of 0.056 L_{Ref} above the surface of the train. Each plate was 1/120 L_{Ref} thick. An example can be seen in Fig. 7 of the standard frontal blocker plates.

The three locations for streamwise placement of the plates were as follows:

- A front plate, positioned 1/24 L_{Ref} downstream of the flat transition section of the model, which merges the nose of the train to the body of the train (8/3 L_{Ref} downstream of nose).
- A middle plate, located at the lengthwise mid-point of the train, 8.60 L_{Ref} from the nose of the train.
- A back plate, located 1/24 L_{Ref} upstream of the transition to the tail region of the geometry (14.56 L_{Ref} downstream of nose).

The purpose of varying the placement of the plates was to determine whether it was preferable to disrupt the flow that resulted in the trailing vortex core formation as early as possible, or whether these structures would reform a set distance downstream of the blocker plates, and hence render the more effective placement further downstream. It was also of interest to examine how the varying boundary-layer thickness seen in Fig. 4(b) would affect both the extent to which the plates would be capable of disrupting the flow, and also to document the expected rise in drag coefficient associated with the introduction of the plates.

Another factor investigated for the blocker plates was the sizing, with four alterations on the standard plate explored:

- A short plate, with a height reduced by one-third when compared to the standard plate (maximum height above train of 0.037 L_{Ref}).
- A tall plate, with height increased by 86% when compared to the standard plate (maximum height above train of 0.104 L_{Ref}).
- A thin plate, with width reduced by 40% to 1/10 L_{Ref}.
- A full plate, which removed the gap present between the standard plate pairing, and thus doubled the spanwise region of interrupted flow (total width of 2/3 L_{Ref}).

The alterations in height were determined by examining the free-stream velocity for flow around the baseline model at the frontal streamwise location for the shortened plate, and the rear streamwise location for the taller plate.

2.4. Methods of quantifying the change in the flow

2.4.1. Drag coefficients

With the drag force experienced by a high-speed train generating the majority of the operational power requirements, it
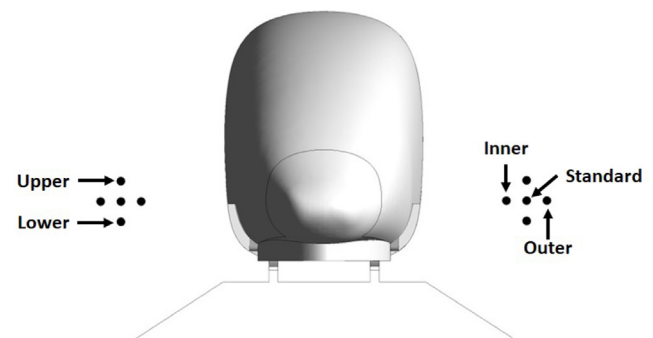

Fig. 8. Location of the five sample lines on each side of the train.

is imperative to monitor and minimise increases in the drag coefficient wherever possible. Additionally, it was of interest to deconstruct the drag coefficient into skin-friction drag and pressure drag components, to better identify the cause of the change recorded in the drag coefficient results. To achieve this, the area-averaged skin-friction coefficient was exported, and normalised by the ratio of reference area, A_{Ref} (the projected frontal area of the train) to actual scale-model surface area. The pressure drag coefficient was subsequently obtained by subtracting the value of the skin-friction coefficient from the total drag coefficient.

2.4.2. Slipstream velocity: General

To obtain the slipstream velocity data, sample lines were generated running from the inlet to the outlet on each side of the train. Originally the only line was the *standard* line, located at the TSI specified position, but in the secondary testing an additional 4 lines, each displaced 0.1 L_{Ref} in either the vertical or spanwise direction, were added, see Fig. 8.

At the end of each timestep the three component velocities (u_x, u_y, u_z) were saved at all nodes along both lines. When the data was later processed, the inlet velocity was subtracted from the x velocity component and the sum of squares used to define the net relative slipstream velocity for each location, at the conclusion of each timestep. Note that by convention, although it was recorded, the vertical (z) velocity component was not used in the calculation of the slipstream velocities. It is defined by

$$U_{Slipstream} = \sqrt{(U_{Ref} - u_x)^2 + u_y^2}$$

where u_x and u_y are the streamwise and spanwise velocity components measured in the train's frame of reference.
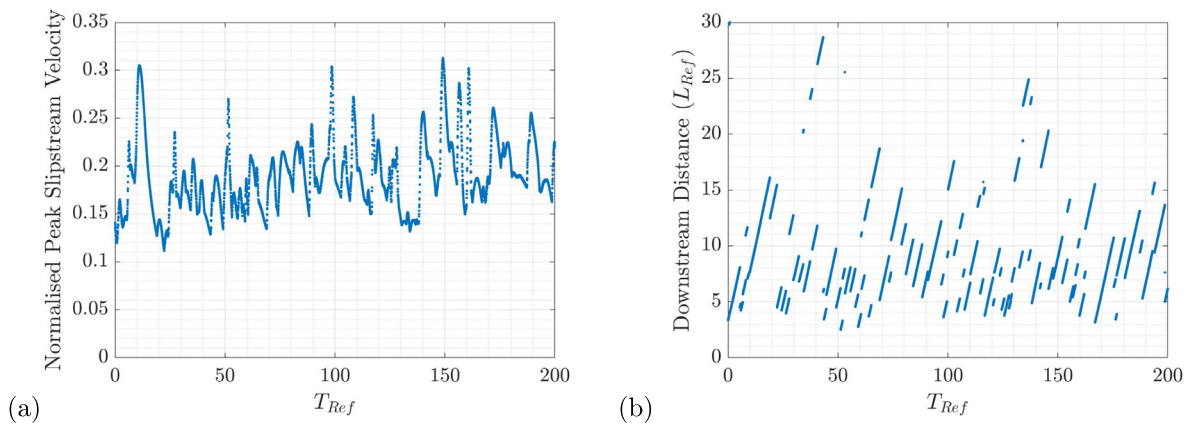
Fig. 9. (a) Values of maximum slipstream velocities at any point on the test lines and (b) the corresponding distance downstream of the vehicle at which they occur for the baseline, clean train model.

2.4.3. Slipstream velocity: Maximums measure of slipstream velocity

Whilst a moving-probes method, which largely replicates the TSI specified slipstream velocity measure, was explored in [21], it proved highly susceptible to variation and fails to take advantage of the ease in which large data sets can be obtained at a far greater number of locations when using CFD, as it was designed with the restrictions imposed by full-scale experimental testing. As such, an alternative measure of the slipstream velocity was developed, which took advantage of the full data set available and provided a more robust indication of induced velocities. Instead of using probes to sample small sections of the test lines, the entire test line was sampled at the conclusion of each timestep, with the maximum slipstream velocity at any point on either line recorded, as well as the corresponding downstream distance of this peak. Fig. 9(a) displays the maximum slipstream velocity recorded using this method for each timestep, over a 200 T_{ref} sampling period, for the baseline case, while Fig. 9(b) shows the corresponding downstream distance.

The *maximums measure of slipstream velocity* was defined as the sum of the mean of the sample of individual peak velocities plus two standard deviations. When presented graphically, the mean slipstream velocity is indicated by a point, with a line extending vertically with a magnitude of two sample standard deviations. The top of this line indicates the value of the slipstream velocity measure. For the fin designs, where the angle is varied, a trend-line is also fitted to the slipstream measure values. An example is shown in Fig. 10.

2.4.4. Slipstream velocity: Downstream location of maximum slipstream velocities

Given the intention of multiple control devices was to redirect the vortex core structures so as to prevent large disruptions from reaching the spanwise location of the test lines, the streamwise locations at which the peak velocities were recorded were also examined. As large flow structures move downstream they may be the cause of the largest slipstream velocity for considerable periods of time, generating the diagonal lines seen in Fig. 9(b). Eventually a new structure will generate a larger velocity, generally closer to the rear of the train, and a new line will commence. The occasions when a location *further* downstream becomes the source of the new largest velocity are illustrative of the meandering nature of the vortex cores, where a significant flow disturbance moves sufficiently in the spanwise direction to coincide with the location of the test lines. Monitoring the mean downstream location of the maximum slipstream velocities is thus useful in determining whether or not these peaks are actually being shifted further downstream.
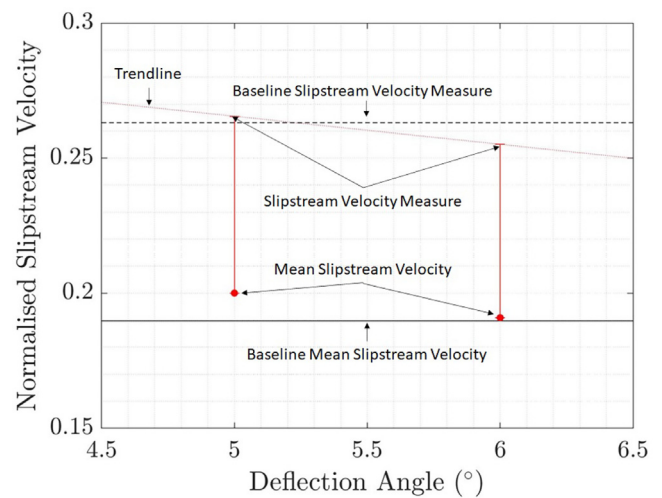

Fig. 10. Example of how the slipstream measure is presented graphically.

2.5. Secondary testing

Refinements to the methodology were implemented for a second series of tests, conducted on the most promising device from each category, as determined by the maximums measure of slipstream velocity.

- The sampling time was increased by a factor of three, from 200 T_{ref} to 600 T_{ref}.
- The number of sampling lines on each side of the train was increased to five, with each shifted 0.1 L_{Ref} vertically or in the spanwise direction from the standard test line, see Fig. 8.
- Resolution was increased around the control devices, with new bodies of influence added to directly surround the control devices. These regions extended 1 L_{Ref} upstream, 2 L_{Ref} downstream and 0.5 L_{Ref} in the spanwise and vertical directions from the edges of each device. The element size within these regions was 1/60 L_{Ref}.
- The *Train Body* body of influence was increased in length from 25 L_{Ref} to 51.66 L_{Ref}, and the height from 2 L_{Ref} to 2.66 L_{Ref}. The change in length was to ensure that the refinement region extended sufficiently downstream to capture all key regions of the wake, with the new length equivalent to the largest downstream distance at which a peak slipstream velocity had been recorded in primary testing. The increase in the height of the region was to ensure that additional
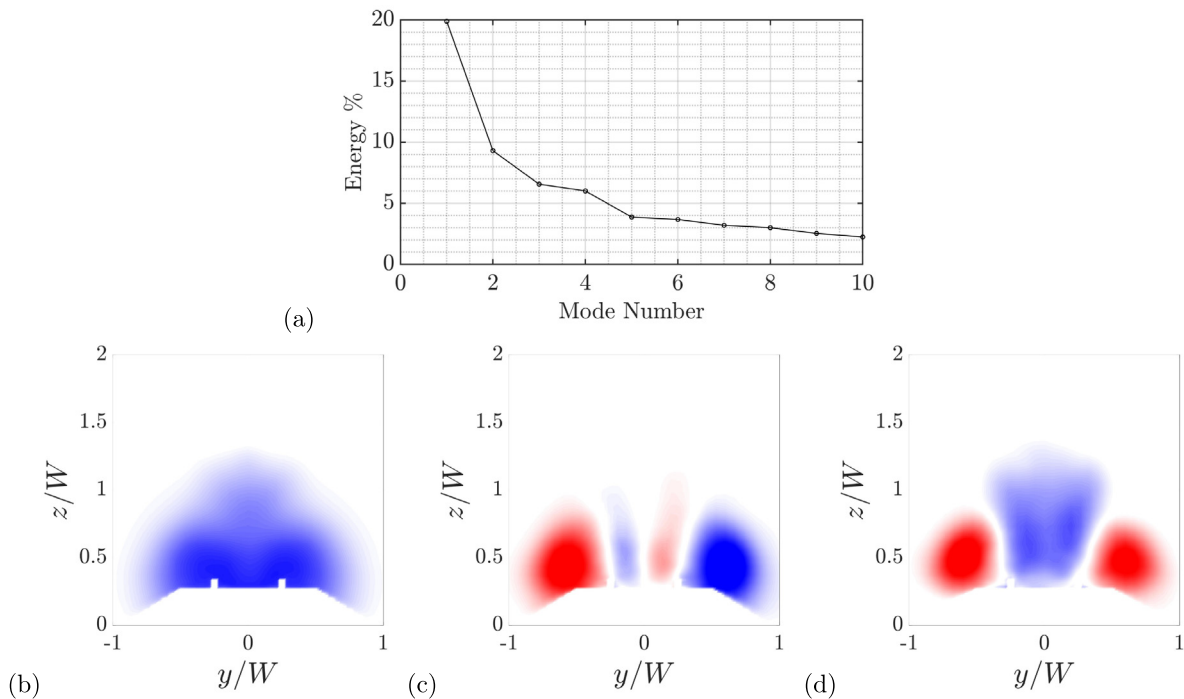
Fig. 11. POD breakdown of the slipstream velocity, showing (a) the energy contributions of the ten most energetic modes of oscillation, (b) the shape of the mean, (c) mode 1 and (d) mode 2 distributions for the baseline train case at a downstream distance of 3 L_{Ref}.

upwash generated by certain control devices, such as the frontal blocker plates, was fully captured.

- The velocity field data was recorded at a range of additional streamwise planes.

These changes were implemented to increase reliability of the predictions, examine sensitivity, improve statistics, and enable a better understanding of how the wake evolves downstream of the tail and in the vicinity of the add-on devices.

2.5.1. POD analysis

The dataset used in the POD analysis was that of the slipstream velocity at eleven vertical planes from 2 to 12 L_{Ref} downstream of the train rear. The deconstruction employed the approach defined in [22]. Each plane for which POD data was exported extended 2 L_{Ref} in both spanwise directions from the centre-plane and 8/3 L_{Ref} from the ground vertically, although when plotted in figures such as Fig. 11 this is trimmed to only show regions of interest. For each test plane, the energy of the equivalent slipstream mode was compared to the corresponding energy for the baseline (clean-train) simulation.

The idea behind POD is the take a time sequence of (typically) velocity fields with the mean removed and find a set of orthogonal fields or POD modes that can be used to reconstruct the original sequence of fields. In this sense, it somewhat resembles Fourier decomposition of a signal into contributions of a set of orthogonal Fourier modes. Moreover, these POD modes are ordered in terms of energy content of the sequence of fields, so, importantly, it is often possible to form a low-order but fairly accurate representation of the time sequence by summing over the first few POD modes. In addition, the POD modes can often be interpreted in terms of physical flow features, and mode pairs out-of-phase by a quarter of a period may be representative of convective structures in a flow.

The method employed for the current analysis is discussed in greater detail below. It follows the snapshot method of Sirovich [23], which is more efficient computationally if the number of

timesteps is smaller than the field length. The first step is to take the initial data, (e.g. slipstream velocity at each node at a downstream distance of 3 L_{Ref}), and sort/interpolate it onto an equally spaced grid. For this study this grid was 161×121. From this two-dimensional vector field a single 19,481 tall column vector is constructed:

$$x(r) = \begin{bmatrix} x(r_{1,1}) & x(r_{1,2}) & \dots & x(r_{1,121}) \\ x(r_{2,1}) & x(r_{2,2}) & \dots & x(r_{2,121}) \\ \vdots & \vdots & \ddots & \vdots \\ x(r_{161,1}) & x(r_{161,2}) & \dots & x(r_{161,121}) \end{bmatrix}$$

$$\rightarrow x(r) = \begin{bmatrix} x(r_{1,1}) \\ x(r_{1,2}) \\ \vdots \\ x(r_{2,1}) \\ \vdots \\ x(r_{161,121}) \end{bmatrix}$$

This column vector is created for each timestep, and represents a snapshot of the data. These snapshots are subsequently compiled into a single data matrix **X**. Hence each column of the matrix contains the vector field at sequential times.

$$\mathbf{X} = \begin{bmatrix} \vec{x}_1 & \vec{x}_2 & \vec{x}_3 & \dots & \vec{x}_{6000} \end{bmatrix}$$

This $M \times N$ matrix **X** can be decomposed into a combination of three new matrices, **U**, **S** and **V**, using *Singular Value Decomposition (SVD)*:

$$\mathbf{X} = \mathbf{U}\mathbf{S}\mathbf{V}^T. \tag{1}$$

Here, **U** has the same shape as the original matrix, and **S** and **V** are both square $N \times N$ matrices, where in this case N corresponds to the number of timesteps. Notably, **S** is a diagonal matrix with the squares of the diagonal elements corresponding to the energies of the orthogonal eigenvectors. These energies are ordered from largest to smallest. The idea is to diagonalise
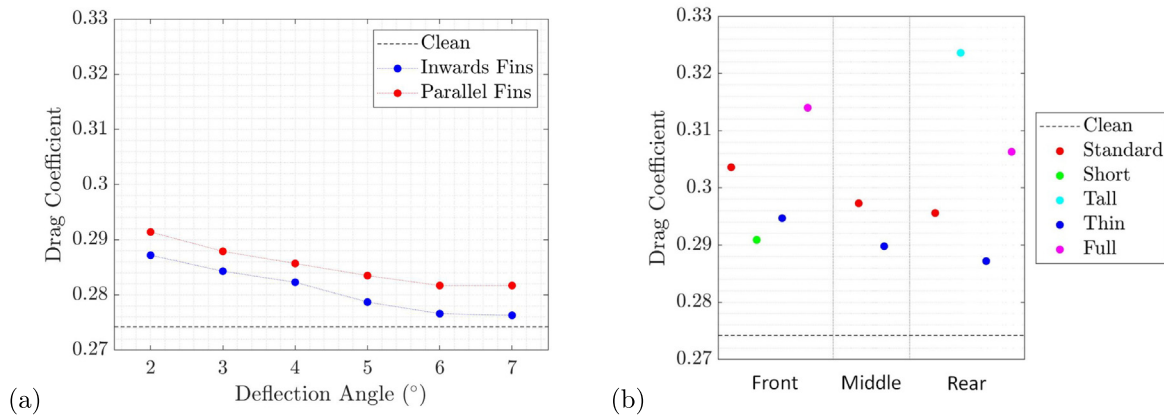
Fig. 12. Drag coefficients for (a) various fin and (b) blocker plate designs.

the correlation matrix $\mathbf{C} = \mathbf{X}^T\mathbf{X}$, which defines the energies and cross-correlations of the fields. Using the SVD for $\mathbf{X}$ given above, this can be expressed

$$\mathbf{C} = \mathbf{X}^T\mathbf{X} = (\mathbf{U}\mathbf{S}\mathbf{V}^T)^T(\mathbf{U}\mathbf{S}\mathbf{V}^T) = \mathbf{V}\mathbf{S}\mathbf{U}^T\mathbf{U}\mathbf{S}\mathbf{V}^T = \mathbf{V}\mathbf{S}^2\mathbf{V}^T \qquad (2)$$

This shows that the eigenvalues of $\mathbf{C}$ correspond to the squares of the diagonal elements of $\mathbf{S}$ with the eigenvectors corresponding to columns of $\mathbf{V}$. Note that this step can be done directly to find the eigenvalues ($\mathbf{S}^2$) and eigenvectors ($\mathbf{V}$) without first doing SVD on $\mathbf{X}$. However, rather than $\mathbf{V}$, the matrix $\mathbf{U}$ is needed for POD reconstruction, and it can be obtained from

$$\mathbf{U} = \mathbf{X}\mathbf{V}\mathbf{S}^{-1} \qquad (3)$$

In fact, the columns of the matrix $\mathbf{U}$ contain the POD modes. Multiplying this matrix by $\mathbf{X}^T$ provides the matrix $\mathbf{A}$, which contains the time series of the coefficients used to reconstruct the sequence of fields from the POD modes. The number of modes is equal to the number of timesteps. In particular,

$$\mathbf{A} = \mathbf{X}^T\mathbf{U} \Rightarrow \mathbf{X}^T = \mathbf{A}\mathbf{U}^T \qquad (4)$$

As indicated, the diagonal matrix $\mathbf{S}^2$ only contains non-zeros in the diagonal cells (i.e., $S_{1,1}, S_{2,2}, \ldots, S_{6000,6000}$) and contains the energy of each mode, ordered from largest to smallest. This matrix is used to create the crucial energy distribution figures such as Fig. 11, and to compare the relative energies recorded for multiple modes and variables for each design. This process was repeated for each of the planes, for each of the required variables, for each design. To check for convergence of the de-compositions, the same deconstructions were conducted over shorter sampling periods of 66.67 T_{ref} and 133.33 T_{ref}. Time-resolved POD deconstructed the set of velocity fields into a set of equivalent modes; in particular, the mean mode and remaining spatial modes ordered by fraction of total energy. Examples are shown for the slipstream velocity of the baseline model at a downstream distance of 3 L_{Ref} in Fig. 11.

A frequency analysis of slipstream mode 1 was also conducted, to identify the effect of the surface additions. The spanwise and vertical shifts in the location of this mode was also examined, with each mode defined as the mean vertical and spanwise loca-tion of the 100 most energetic grid elements, in both negative and positive directions (see Fig. 11(c)), for each plane. Finally, mean slipstream and spanwise velocity differential analysis was under-taken, to provide a visual representation of regions of increased or decreased energy in the wake when compared to the baseline case, by subtracting the baseline mean energy distribution from that generated for each case. For this the flow was analysed at the vertical plane 3 L_{Ref} downstream and a horizontal plane which was placed at the standard test height (0.4 L_{Ref} above the

platform) and extended from 2 L_{Ref} to 12 L_{Ref} downstream in the streamwise direction and 2 L_{Ref} in both spanwise directions from the centreplane.

2.5.2. X-vorticity

As a final means of visualising the flow, the time-averaged x-vorticity was utilised in the secondary testing. By limiting the vorticity to only that occurring in the plane perpendicular to the streamwise direction, a strong visual indication of the counter-rotating vortex cores was obtained and compared to the baseline case in the near-field wake.

3. Results - preliminary tests

3.1. Drag coefficients

Fig. 12 indicates that all devices tested increased the drag from the baseline value, although the extent of this increase varied considerably.

For both sets of fin designs, Fig. 12(a) shows that the drag decreases as the deflection angle rises. Table 7 indicates that this is due to the pressure drag decreasing, while the skin friction drag remains relatively constant. The parallel fins follow a similar profile, but produce a considerably greater drag rise at all angles, with the pressure drag appearing to plateau at large deflection angles.

The blocker plates of Fig. 12(b) generally produce considerably greater drag rises, with only the thin rear blocker returning a drag coefficient lower than any of the fin designs. Positioning the plates further downstream reduced the extent of the drag increase, as more of the plate became enveloped in the boundary layer which had developed along the roof of the model. Unsur-prisingly, the drag increased or decreased relatively proportional to the increase or decrease of the size of the plate, with height alterations having a larger effect than width variations, again due to boundary layer effects.

3.2. Slipstream velocity

For the inwards deflected fins of Fig. 13(a), only one case, at 6°, produced a reduction in the measure. A trend of decreasing measure with increasing deflection angle is generally observed until 6°, with a sharp rise occurring at 7°. It is also of note that the reduction recorded at 6° has an almost identical mean value to the baseline, and thus the decrease is due to a reduction in the standard deviation, potentially indicating fewer dangerous slipstream velocity excursions.
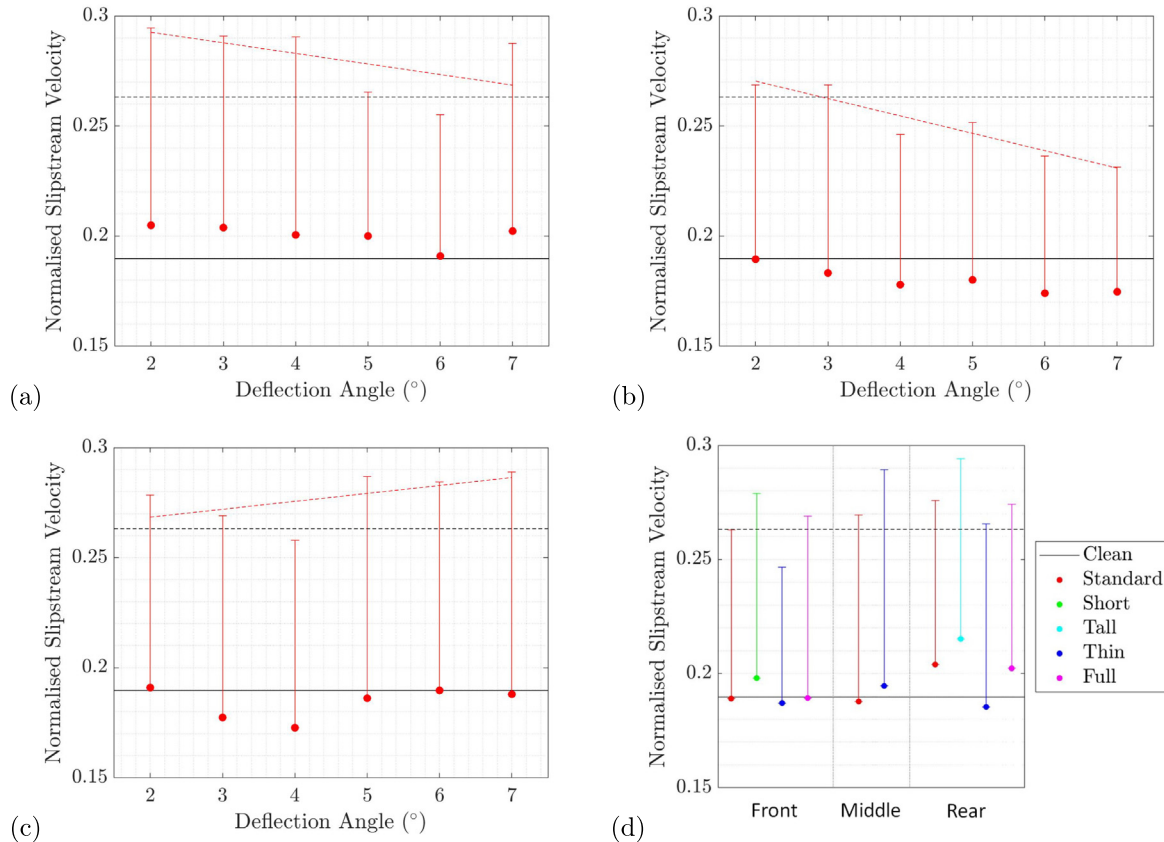
Fig. 13. Slipstream velocity for (a) inwards deflected fins, (b) parallel fins – *passenger side*, (c) parallel fins – *danger side* and (d) blocker plates.

The results for the parallel fins, shown in Fig. 13(b) and (c), appear far more promising, with consistently large reductions of over 5% recorded from 4° upwards on the *passenger side* (Fig. 13(b)), peaking at a 12% reduction at 7°. Even at the small deflection angles, where increases in the measure are recorded, these are less severe than those seen at equivalent deflections for the inwards fins. Additionally, for all six cases, the mean slipstream velocity is below that of the baseline. As anticipated, on the *danger side*, Fig. 13(c), the measure increases a relatively equivalent magnitude to the decreases recorded on the *passenger side*, particularly at the larger deflection angles, highlighting the obvious limitation of this design. However, it is interesting to note that for the majority of cases the mean slipstream velocity is below that of the baseline, with the measures increasing due to larger standard deviations.

Of the blocker plate designs displayed in Fig. 13(d) only the thin front design produces a significant decrease of 6.3%, however multiple designs produce measures approximating that of the baseline. The frontal location appears to be the most promising, with some significant increases recorded at the middle and rear locations. In terms of the effect of the size variations, reducing the width of the plate appears to improve performance at the frontal and rear location, but not for the central plate, where the measure increases significantly. Increasing the width appears to have minimal effect, and thus is of little interest due to the dramatic drag increase. Both height alterations also resulted in increased measures, with the short and tall plates returning the highest measure at the frontal and rear locations respectively.

3.3. Slipstream velocity: Downstream location of the slipstream maximum

The inwards fins of Fig. 14(a) show a limited ability to restrain large velocity peaks from reaching the spanwise testing positions, with only the fins at 6° shifting the mean value further downstream.

Interestingly, this 6° case is the only design for which the slipstream velocity measure decreases, indicating that there may be a link between the two metrics as hypothesised. However, it does appears that the inwards fins are not an overly successful means of restraining the flow in this manner.

In contrast, the parallel fins demonstrate a clear ability to push the peak velocities further downstream on the *passenger side* as seen in Fig. 14(b), with the mean distance at which peak velocities are recorded observed to be up to 5 L_{Ref} further downstream. Again it can be seen that the angles at which the distance is increased (4° and greater) correspond with the angles at which the slipstream measure decreases. This indicates that the parallel fins are limiting the ability of the largest flow disruptions to reach the test location in the near wake, as desired. On the *danger side* the peaks remain close to the baseline and have small variation, indicating that large flow disturbances are consistently and frequently extending to the test line.

Unlike the fin designs, the blocker plates did not aim to restrain the flow from extending out to the test locations, and as such are not shown, however these values are provided in the Appendix in Table 9.
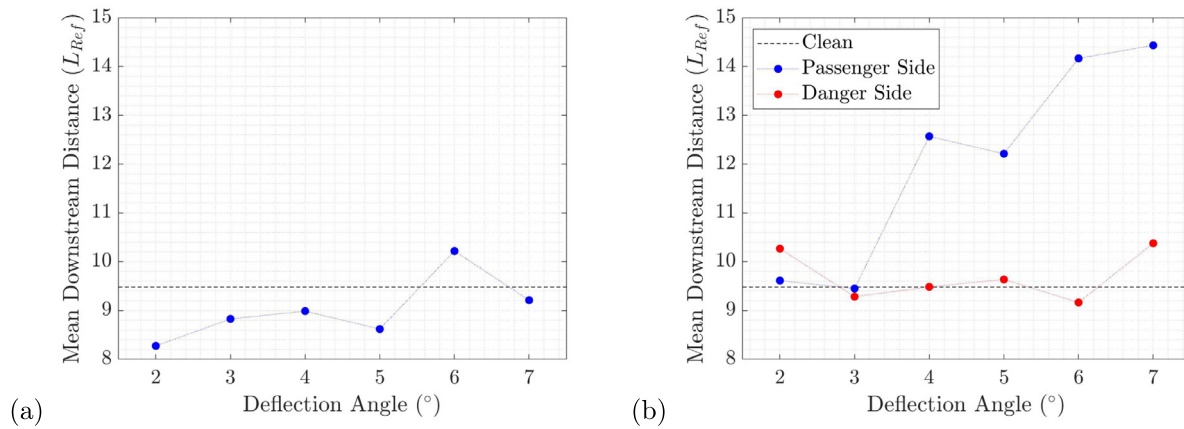
Fig. 14. Downstream location of maximum slipstream velocities for (a) inwards deflected fins and (b) parallel fins.

3.4. Summary of preliminary testing

3.4.1. Inwards deflected fins

The inwards deflected fins demonstrated a limited ability to reduce the occurrence of large slipstream velocities through restraining the counter-rotating vortex cores to the region directly behind the train. Only the 6° deflected fins decreased the slipstream measure and shifted the mean peak velocity location further downstream. However, of the three design classes, the inwards fins produced the most modest drag increases, particularly at the more promising, larger deflection angles.

3.4.2. Parallel fins

The parallel fin designs demonstrated a far greater capability to generate a reduction in the measure of slipstream velocity, due to a significantly improved ability to shift the peak velocity locations further downstream on the *passenger side* of the train. Unfortunately, these designs also increased the measure noticeably on the *danger side* and produce a significantly larger drag increase than the inwards deflecting fins for equivalent deflection angles, indicating that the ability for the parallel fins to retract when not in use is of significantly greater importance.

3.4.3. Blocker plates

The blocker plates include the smallest surface additions explored, and thus the most plausibly retractable (or foldable) designs. This is crucial, as even the smallest plates produce significant drag increases. However, the thin front blockers reduced the slipstream velocity measure by a substantial 6.3%, outperforming any of the inwards deflected fin designs. This reduction appears to be due to a weakening of the trailing counter-rotating vortex cores. Hence, these results suggest the key to this energy reduction is to disrupt the flow that feeds these structures, by increasing vorticity in the regions above the roof of the model, as seen in Fig. 15.

This explains the greater effectiveness of plates located at the frontal position, where the natural flow upwash causes the eddies shed around the edges of the plate to propagate downstream at a greater height.

4. Secondary tests

The most successful design, as determined by the measure of slipstream velocity, from each of the three design classes were subsequently examined in greater detail against the baseline case.

The designs chosen for further analysis were:

- For the inwards fin designs, a deflection angle of 6°.

Table 5
Drag coefficients and drag variation from the baseline case for new and old testing parameters.

Design case	C_D	New ΔC_D (%)	Old ΔC_D (%)
Baseline	0.2701	–	–
Inwards deflected fins - 6°	0.2733	1.21	0.88
Parallel fins - 7°	0.2794	3.47	2.75
Thin front blocker plates	0.2904	7.51	7.50

- For the parallel fin designs, a deflection angle of 7°.
- For the blocker plates, the reduced width, forward located plates.

4.1. Drag coefficients

Table 5 shows the drag values for the cases following the updates to the experimental method. Firstly, it can be observed that the drag coefficients obtained from the enhanced methodology are all marginally reduced by around 1% when compared to values from the original tests (compare Tables 1 and 5). This may be contributed the increased mesh resolution capturing flow separation regions near the rear of the model.

The relative drag rise for each design, in comparison to the new baseline value, is less dramatically affected, increasing by 0.72% for the parallel fins at 7° deflection, 0.33% for the inwards fins at 6° deflection and only 0.01% for the thin front blocker plates.

4.2. Slipstream velocity and mean downstream distance of maximum

Fig. 16 indicates that all three devices remain promising with regards to their ability to decrease this slipstream measure. At the original test lines (a), the inwards fins record a 7.4% reduction over the baseline case, a significant improvement from the previous value of 3.0%. Similarly, the *passenger side* parallel fin case improves from a 12.1% to a 19.8% slipstream reduction, further establishing itself as the most effective design at reducing this measure. More dramatic, however, is the manner in which the *danger side* measure is altered from a substantial 9.8% rise, to a fairly neutral 1.1% reduction. This is particularly surprising given the consistency at which this measure increased significantly on the *danger side* of the previous parallel fin tests at all deflections greater than 4°. This may indicate that the increased mesh refinement around the fins is capturing the flow behaviour more accurately, and that there may now be a disruption to the counter-rotating vortex cores at large deflection angles, similar
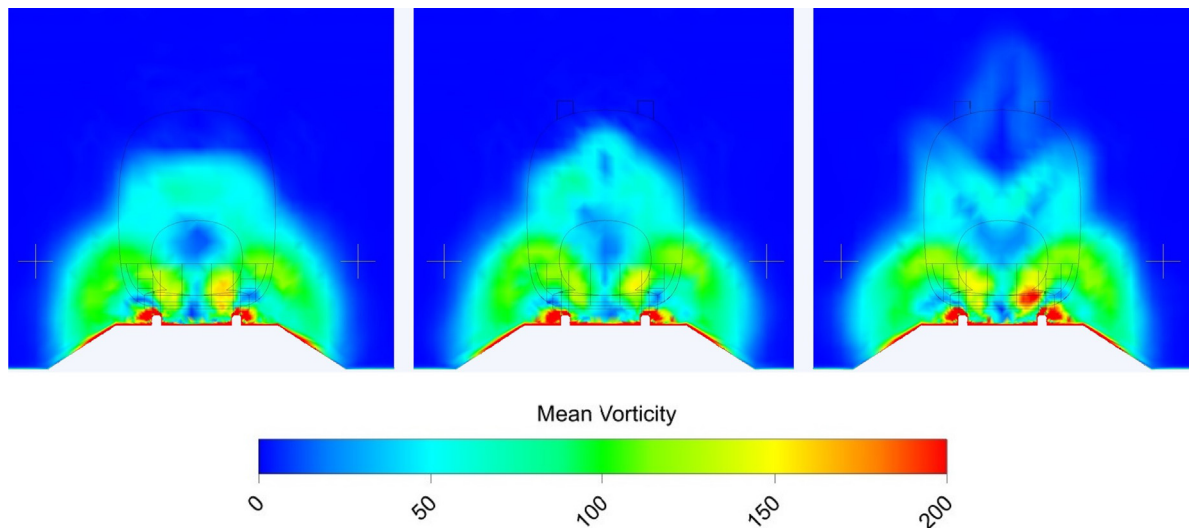
Fig. 15. Mean flow vorticity 3 L_{Ref} downstream of the rear of the train, for clean train, thin back blockers and thin front blockers (left to right). Test locations are indicated by yellow crosshairs. (For interpretation of the references to colour in this figure legend, the reader is referred to the web version of this article.)
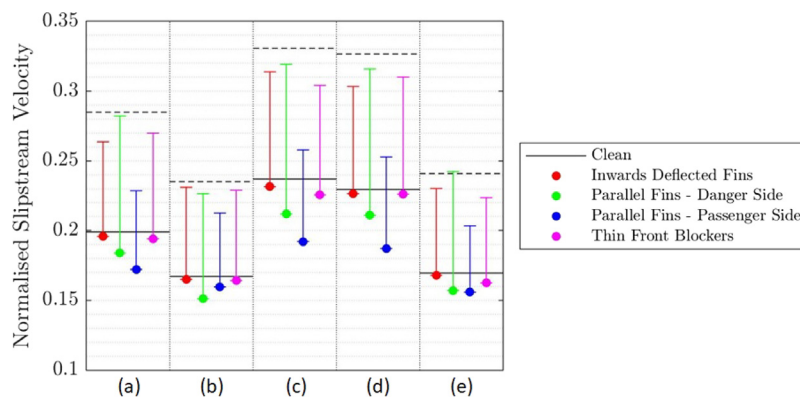

Fig. 16. Slipstream velocity measures recorded along (a) standard line, (b) upper line, (c) lower line, (d) inner line and (e) outer line.

Table 6
Variation on baseline of mean downstream distance of peak slipstream velocities, in units of L_{Ref} from rear of model.

Design case	Standard	Up	Down	In	Out	Mean	%
Inwards deflected fins	0.01	−0.44	0.31	−0.52	−0.34	**−0.20**	**−1.66**
Parallel fins - *Passenger Side*	5.64	4.86	4.18	4.92	6.39	**5.20**	**50.02**
Parallel fins - *Danger Side*	−0.43	−1.24	1.80	0.42	−0.13	**0.09**	**2.44**
Thin front plates	0.29	−0.26	0.27	−0.59	−0.25	**−0.11**	**−0.96**

to that observed with the blocker plates. Finally, the thin front blockers return a 5.2% reduction, down marginally from the 6.3% recorded in the primary tests.

With regards to the new test lines, it can be seen that the upper (b) and outer (e) lines consistently record lower measures than the standard (a) line, while the lower (c) and inner (d) lines have more intense slipstream velocities.

The results of the new test lines were generally predicted quite well by the standard test line, for example, at all five locations the *passenger side* of the parallel fins records the greatest reduction, ranging from 9.6% at the upper line to 22.6% at the inner line. There are, however, some notable variations between the test lines for the other devices, with changes in the order of the magnitude of reductions. The inwards deflected fins are the second most effective at the standard and inner location (a and d), the thin front blocker plates second most effective at the lower and outer locations (c and e), and, surprisingly, the *danger side* of the parallel fins second most effective at the upper location (b).

Finally, it is of note that only at the outer line is any increase in the measure recorded for the *danger side* of the parallel fins, further suggesting a disruption to the counter-rotating vortex cores.

With regards to mean downstream distances presented in Table 6, the inwards fins and thin front blockers again appear to be ineffective at shifting the peaks further downstream at any of the test locations, with the average shift less than 2%. In contrast, the parallel fins are extremely effective at shifting the peaks on the *passenger side* further downstream at all five test lines, with the increase in distance of 55% at the standard line up marginally from 52% from the initial testing stage and an average shift of 50% recorded across the five locations. Interestingly, while on the *danger side* the average shift across the five locations was small, there is a clear shift closer to the tail at the upper location, and further downstream at the lower location, indicating noticeable variation in the vertical direction for this case.
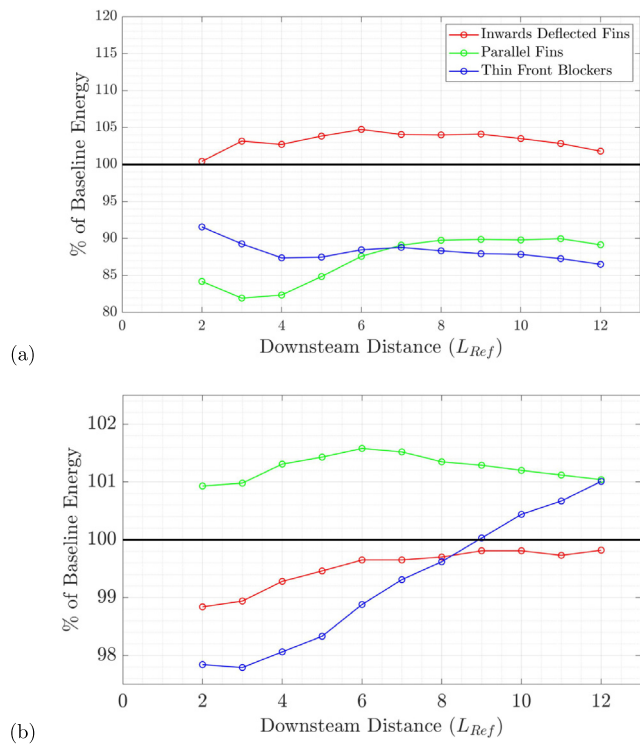
(a)

(b)

Fig. 17. Relative energy of (a) mode 1 and (b) total energy for the three design variations in comparison to the baseline.

Fig. 18. Non-dimensionalised mean slipstream velocity differential for inwards deflected fins at a downstream distance of 3 L_{Ref}. (For interpretation of the references to colour in this figure legend, the reader is referred to the web version of this article.)

4.3. POD: Relative energy analysis

From Fig. 11, the counter-rotating vortex cores were clearly identified as the primary wake mode affecting slipstream velocity, with an average energy contribution of 20% constituting more than double the energy of the second most energetic mode. Very similar spatial distributions occurs in the primary mode for all four geometries tested, and thus an analysis of the comparative energy of all modes, with a particular focus on this primary mode, was conducted. The energy of the first mode, as well as the total energy, obtained from the sum of all the modes, including the mean, is summarised below in Fig. 17(a) and (b).

Fig. 17(a) provides the strongest evidence yet that the success of the forward positioned blocker plate designs is due to a weakening of the counter-rotating vortex cores which constitute the most energetic mode. The thin front blocker plates produce a steady decrease of between 8 and 14% in the energy of this mode, the largest at the six furthest downstream planes. Additionally, as observed in Fig. 17(b), these devices produce the largest decrease in the total energy in the near wake, with a 2.2% reduction dissipating as the flow moves downstream, with the trend resulting in minor increases at the three most distant planes.

What is more surprising is that the parallel fins are, on average, even more effective at reducing the mode 1 energy, particularly in the near wake, with reductions of up to 18%. This may explain the reduction in the slipstream measure recorded at 4 of the 5 test lines on the *danger side*, as the energy of the counter-rotating cores is significantly diminished. However, unlike the thin front blocker plates, the parallel fins generated an increase in the total energy at all planes, indicating that the large surfaces are creating a number of smaller scale disturbances which lead to an overall increase in the energy of the wake.

Finally the inwards deflected fins cause a minor *increase* in the mode 1 energy, likely due to the vortex core structures being
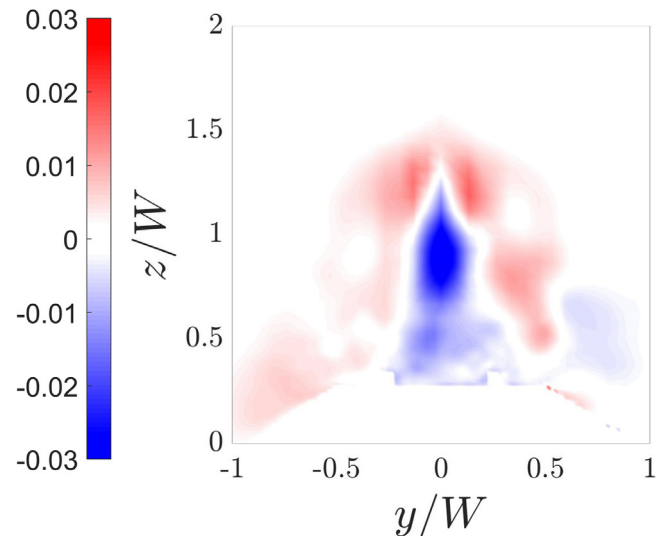
forced into closer proximity, however a steady, albeit minor, decrease is recorded in the total energy at all planes.

4.4. POD: Mean velocity differential analysis

POD analysis was also utilised to provide a visual illustration of the change in the wake flow generated by each control device. The flow differences generated by the control devices can be difficult to observe by merely showing the POD energy distributions. As such, the difference in the mean energy distribution between each case and the baseline was constructed by subtracting the baseline distribution from that of each case. These are presented at two planes, the vertical plane used for the standard POD analysis at downstream distance of 3 L_{Ref} and a horizontal plane at the reference height of 0.4 L_{Ref} above the platform. This provides an illustration of the regions in the wake where the energy was increased or decreased relative to the baseline, generally for the slipstream velocity, but also for the spanwise velocity for the parallel fin case.

4.4.1. Inwards fins - 6 degrees deflection

Fig. 18 shows the differential profile, which illustrates a central region of reduced mean slipstream velocity (blue), surrounded by regions of increased velocity (red). This suggests that the redirected flow is reducing the slipstream velocity by creating less of a streamwise velocity deficit in the near wake, with a maximum reduction equivalent to 3.5% of U_{Inlet}. Given that the mean slipstream velocity of the baseline flow at this location is approximately 0.2 U_{Inlet}, this represents a sizable reduction of 17%. This is also nearly twice the magnitude of the greatest velocity increase of 1.9% of U_{Inlet}.

Despite being located below the region of largest mean slipstream reduction shown in Fig. 18 the horizontal plane of Fig. 19 shows a clear region of energy reduction in the direct wake, bracketed by regions of energy increase. The magnitude of this decrease is largest approximately 4 L_{Ref} downstream, where the reduction is just under 2%. Both these results match with the reduction in the total slipstream energy recorded at all test planes for this case, however, this arrangement is not ideal for improving bystander safety, as the energy reductions are present directly behind the train while the energy is increased at greater spanwise displacements where bystanders are likely to be positioned.
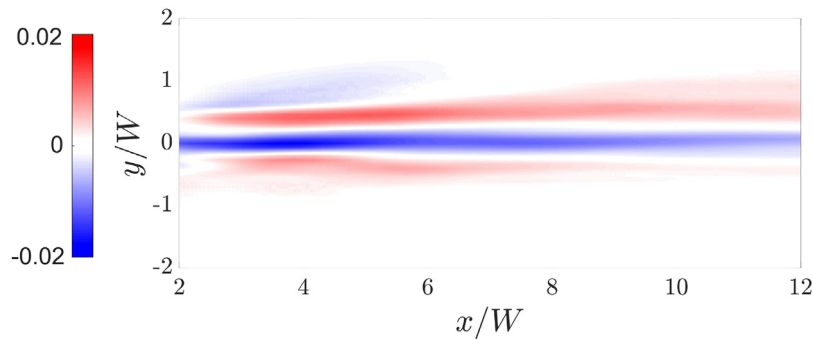
Fig. 19. Non-dimensionalised mean slipstream velocity differential for inwards deflected fins at standard test height.
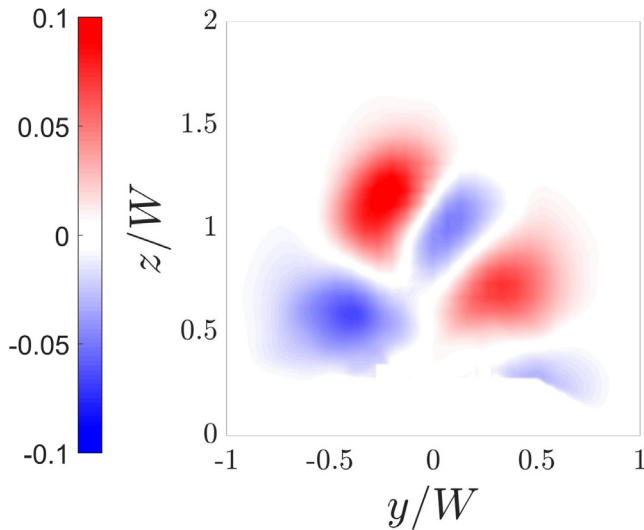

Fig. 20. Non-dimensionalised mean slipstream velocity differential for the parallel fins case at a downstream distance of 3 L_{Ref}. (For interpretation of the references to colour in this figure legend, the reader is referred to the web version of this article.)

4.4.2. Parallel fins - 7 degrees deflection

As expected, the parallel fins produce an asymmetric distribution, as seen in Fig. 20.

The red regions appear to show the new locations of the vortex-core structures after redirection to the *danger side* (right of image) by the fins, while the blue region on the *passenger side* illustrates where this structure is for the unmodified train. Unlike the inwards fins, the peak increase of 10.0% exceeds the peak velocity decrease of 6.6%, with the magnitude of these changes illustrating the far more dramatic impact of these fins. As the regions of energy increase are larger, and of greater intensity, than those of energy reduction, it explains why this device was the only one to increase the total slipstream energy at this downstream distance, as seen in Fig. 17(b).

In the horizontal plane, examining the spanwise velocity is of greatest interest, to determine if the fins are indeed shifting the flow away from the *passenger side*.

Fig. 21(a) shows that for the baseline case the flow moves away from the centreplane in both directions evenly. However, for the parallel fins case shown in Fig. 21(b), the overwhelming majority of the region shows flow only moving in the positive *y*-direction, towards the *danger side*. In particular there is significantly stronger spanwise flow in the far wake. The differential profile of Fig. 21(c) shows that the change in spanwise velocity is focused around the centreplane, and maintains its intensity

well as it moves into the far wake. This provides clear evidence that the parallel fins are having a significant spanwise redirection effect as desired, and that this is acting well into the far field.

4.4.3. Thin front blocker plates

The distribution seen in Fig. 22 follows on from that previously shown in Fig. 15, where large areas of additional flow disruption are observed in the region above the roof of the train.

Here this is seen in the large regions of increased slipstream velocity directly above, and to either side of the train. Interestingly, there is also a large region of reduced slipstream velocity, directly in the wake of the train with the peak magnitude of this reduction 5.6% of U_{Inlet}, significantly larger than the similar reduction recorded in this region for the inwards deflected fins, albeit over a smaller region. This matches with this device recording the largest decrease in total slipstream energy at this downstream location, see Fig. 17(b). It also explains why the smallest reduction in the slipstream measure is recorded at the upper test line, as this height is beginning to reach into the regions of significantly increased mean slipstream energy. This reinforces the theory behind the utility of these devices, to reduce energy in the direct wake by adding energy to the flow at heights exceeding that at which any bystander would be positioned.

As with the inwards deflected fins, the majority of the change to the wake occurs above the standard test height. However, Fig. 23 does show that at this height reductions are present throughout the majority of the sample region, while noticeable areas of increase only appear around 6 L_{Ref} downstream.

4.5. POD: Slipstream mode 1 location shift

The parallel fin case had already been observed to shift the downstream distance at which maximum slipstream velocities were recorded in both Fig. 14(b) and Table 6. As such, the spanwise and vertical location of the slipstream mode 1 for each downstream plane was calculated to compare to the baseline. Whilst similar shifts were not observed for the other two cases they were also examined as a point of comparison.

Fig. 24(a) shows a clear spanwise shift on both sides of the model, both of which increase with downstream distance. On the *passenger side* this displacement is towards the centreplane, peaking at a 16.4% reduction in spanwise spread, while on the *danger side* it is away from the centreplane, peaking at a 10.7% increase in spanwise spread. As such, it is promising to note that this change on the *passenger side* is consistently larger than on the *danger side*, shifting an average of 75% further in the far wake (from 7 L_{Ref} to 12 L_{Ref}). It is also interesting to note that there is a consistent vertical shift, with the mode 1 structures shifted down on the *danger side* and up on the *passenger side*, with the magnitude varying less with downstream distance than for the spanwise shift. These shifts also help explain the slipstream
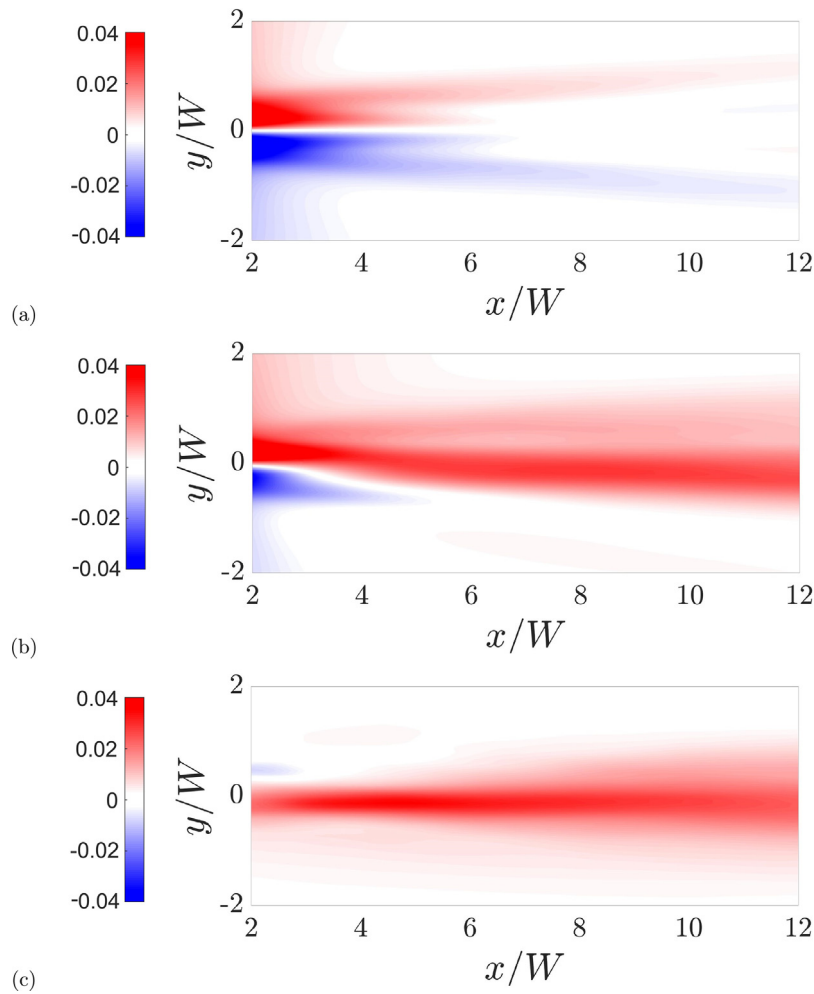
Fig. 21. Non-dimensionalised mean spanwise velocity at standard test height for (a) baseline case, (b) parallel fins case and (c) the differential of the baseline and parallel fins.
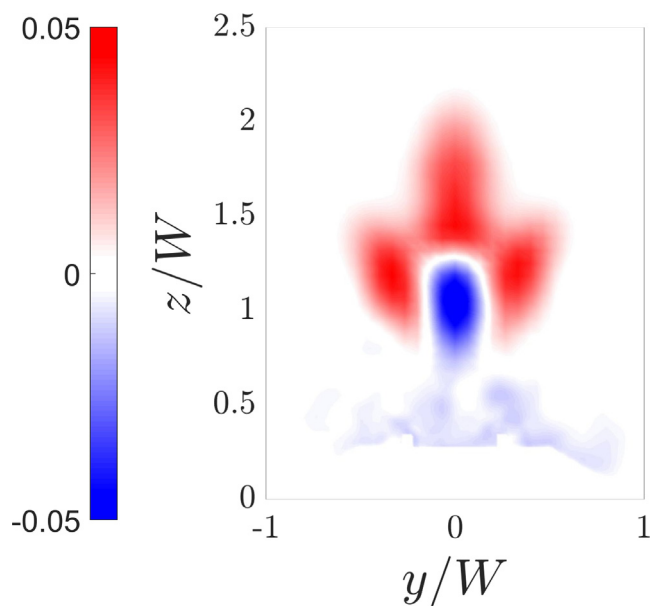

Fig. 22. Non-dimensionalised mean slipstream velocity differential for the thin front blocker plates at a downstream distance of 3 L_{Ref}.

measure results on the *danger side*, with a vertical shift down resulting in the improved performance at the upper test line and the shift away from the centreline corresponding with the only increase in the measure at the outer test line.

In contrast, the other two cases shown in Fig. 24(b) show no clear ability to shift the location of the mode 1 structures in either direction, particularly in the near wake. This is unsurprising for the thin front blocker plates, which did not aim to shift these structures, but the inwards fins are again disappointingly ineffective at producing any spanwise restriction in the near wake.

4.6. POD: Slipstream mode 1 frequency analysis

The addition of the control devices was also capable of significantly altering the frequency response, with mean Strouhal numbers of 0.186, 0.154 and 0.196 returned for the inwards deflected fins at 6° deflection angle, parallel fins at a 7° deflection angle and thin front blocker plates respectively across the 11 sample planes. Examples of these distributions are shown in Fig. 25 at a downstream distance of 3 L_{Ref}.

The thin front blockers of Fig. 25(d), demonstrate an ability to disrupt oscillation of the vortex pair, noticeably flattening the frequency response of the slipstream mode 1. Interestingly, the parallel fins, Fig. 25(c), have the opposite effect, increasing the magnitude of the peak whilst decreasing the magnitude of the
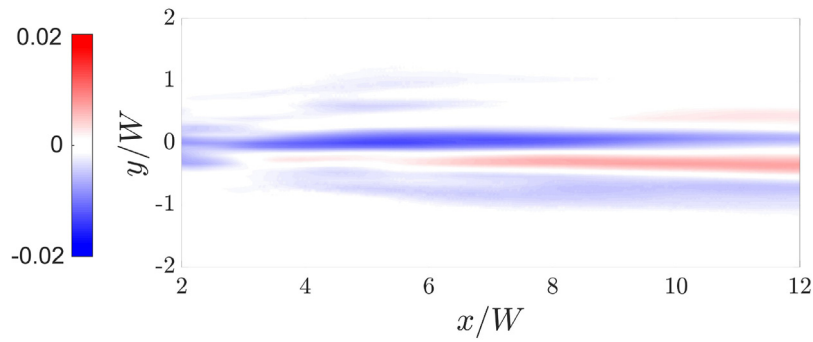
Fig. 23. Non-dimensionalised mean slipstream velocity differential for thin front blocker plates at standard test height.
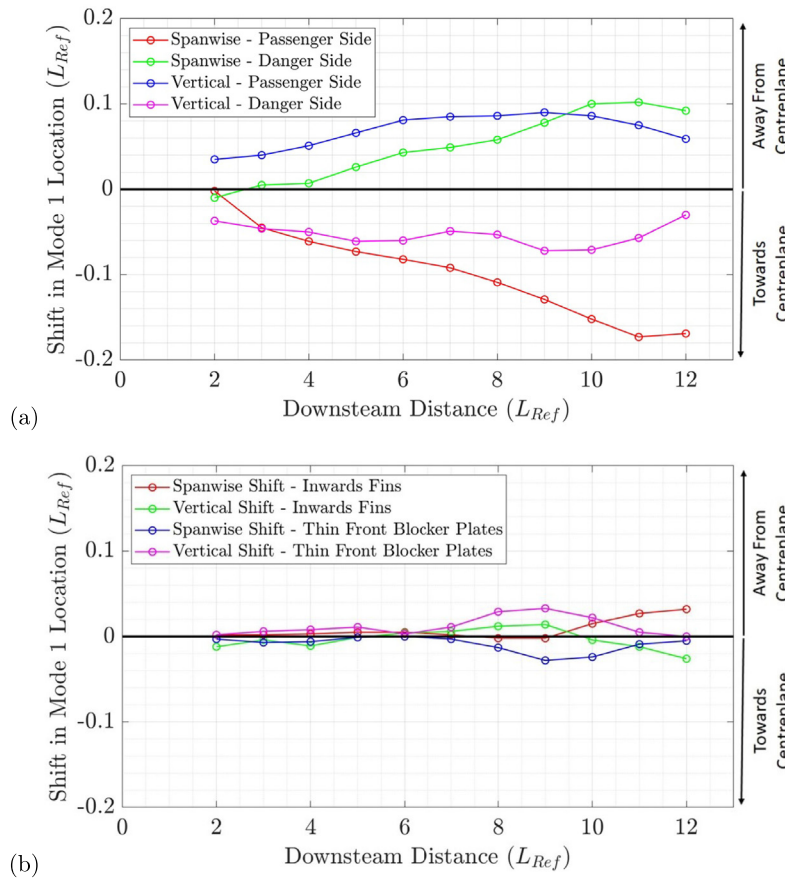

Fig. 24. (a) Shift in spanwise and vertical location of slipstream mode 1 structures on the *passenger* and *danger side* of the train for the parallel fins at 7 degrees deflection. (b) Mean shift in spanwise and vertical location of slipstream mode 1 for the inwards fins at 6 degrees deflection and thin front blocker plates. Note that the convention used is a positive spanwise shift is away from the centreplane, while a negative shift is towards the centreplane.

surrounding regions, indicating that the flow redirection is reinforcing the frequency response, and thus creating more energetic spanwise oscillations in the wake. Thus, while the parallel fins may be decreasing the energy contained within of the vortex pair, and shifting them away from the *passenger side*, they appear to be causing them to oscillate with greater intensity. Finally the inwards fins of Fig. 25(b), vary the profile little from the baseline, other than a slight increase in the mean Strouhal number.

4.7. Flow visualisation: Near wake X-vorticity for parallel fin case

As a final means of examining the near wake flow of the parallel fin case, which is clearly having the most significant impact of the three devices examined, the time-averaged *x*-vorticity was calculated, and is compared to the baseline in Fig. 26. As seen

on the left side of Fig. 26(a), the pair of counter-rotating vortex cores can be clearly identified for flow around the baseline model. It should be noted that the *danger side* is now to the left of the image and the *passenger side* to the right of the image, the reverse of Fig. 20, as the *x*-vorticity figures require a downstream view to observe the flow over the tail region.

At 0.1 L_{Ref} upstream of the tail (Fig. 26(a)), the vortex core on the *passenger side* has grown significantly, and is shifted towards the centreplane and further from the ground when compared to the baseline case. This results in the region combining with the matching vorticity shed from the fins. On the *danger side*, the region is elongated, and has already begun moving lower and further from the centreplane, down the side of the tail. Additionally, a large, intense region of negative x-vorticity is forming near the height of the roof from the direct wake of the fins.
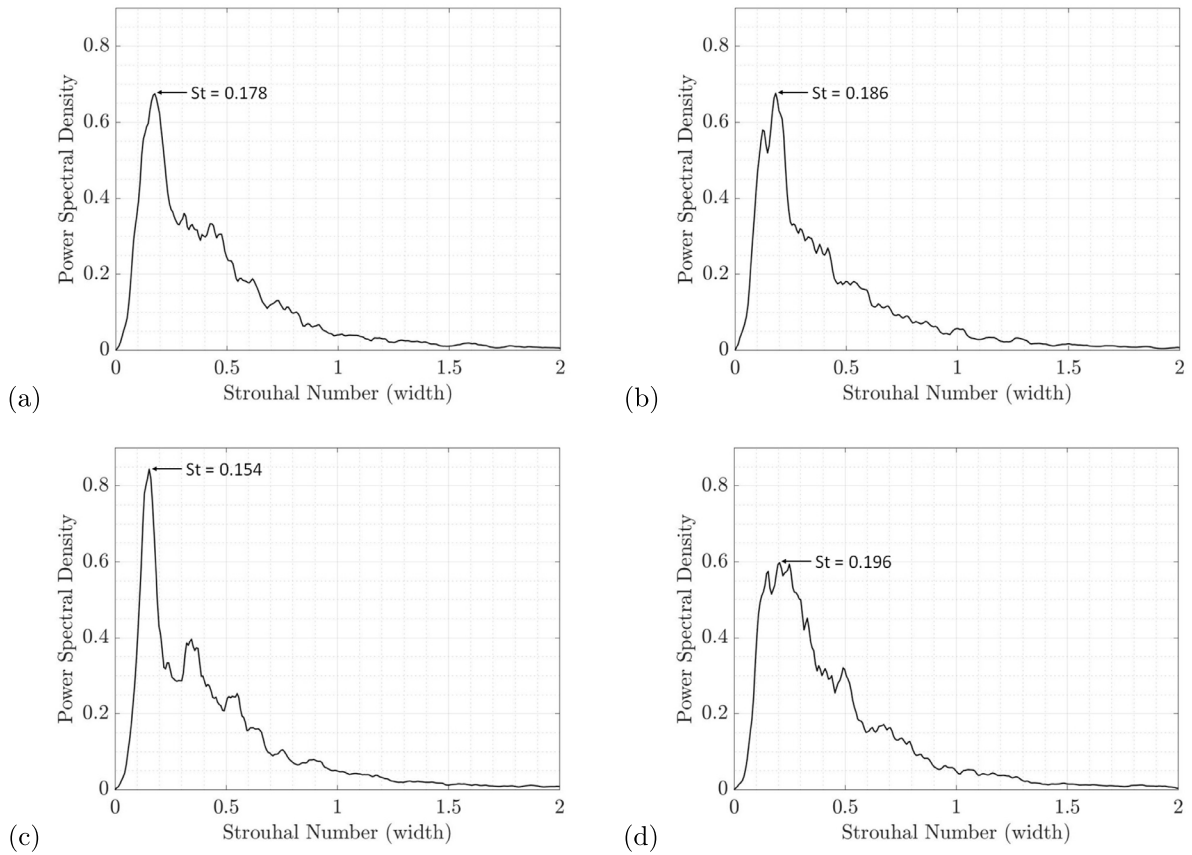
Fig. 25. Power spectral density plots of mode 1 slipstream at downstream distance of 3 L_{Ref} for (a) baseline, (b) inwards deflected fins, (c) parallel fins and (d) thin front blocker plates.
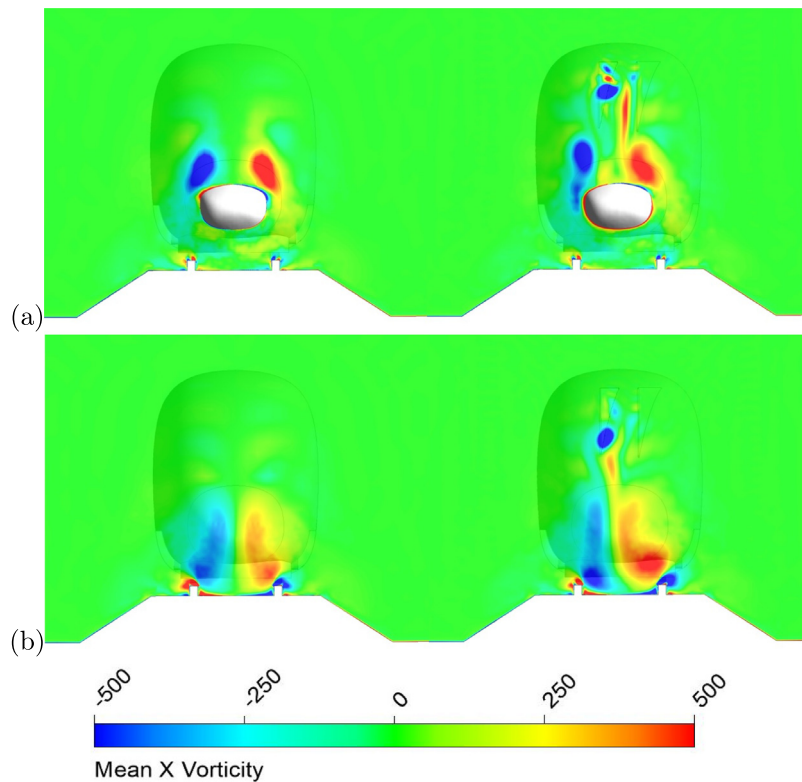

Fig. 26. Mean x-vorticity comparison of baseline (left) and parallel fins (right) at planes located (a) 0.1 L_{Ref} upstream of tail and (b) 0.5 L_{Ref} downstream of tail. (For interpretation of the references to colour in this figure legend, the reader is referred to the web version of this article.)

These trends continues into the downstream region, where at 0.5 L_{Ref} downstream of tail (Fig. 26(b)) the red, *passenger side* region has begun overtaking the blue, *danger side* region, with noticeable higher vorticity intensity. The initial *danger side* core is reduced in size, while the fin wake region is shifting lower and further off towards the left of the figure, maintaining its intensity and dissipating less than the base vortex-core regions. This explains the reduction in mode 1, but increase in total slipstream energy for this case, as while the *danger side* vortex core is weakened significantly, the high vorticity structure shed from the fins increases the overall energy.

5. Conclusions

It has been demonstrated that by adding stationary surfaces to an ICE-3 high-speed train model, the slipstream velocities potentially experienced by passengers can be reduced, through either redirecting, or disrupting the formation of, the primary vortex core structures and in turn reducing spanwise excursions of the high-speed trailing wake flow. However, unfortunately but not unexpectedly, an increase in drag coefficient is observed with all potential designs tested.

Some concerns that could be examined in future work would be determining how effective the disruption generated by the front mounted plates would be on a model that more accurately represents the aspect ratio of a multiple carriage high-speed train. For example, whether the disruption would prove more effective a single carriage from the tail of the geometry, or if the upwash present at the nose of the train is essential for adequately elevating the turbulent flow. Alternatively, if redirecting the flow vertically is key to vortex pair disruption, reclining the plates to further encourage upwash could be explored, as could using jets to inject bursts of high velocity air into the flow at specific locations along the train geometry.

Additionally, the structural stresses experienced by these physical surfaces has not been investigation, neither has the means by which retraction or folding would be employed, to allow operation at high speeds. This could also extend to the additional side forces that could be experienced, both in cross-winds, and for the case of the asymmetric parallel fins, normal flow conditions, when these devices are activated.

Future studies focusing on generating increased upwash may also need to examine the effect that redirecting the turbulent flow upwards has on pantographs, overhead power-lines and other similar structures located in this region. Alternatively, the effect of the slipstream control methods investigated within this study could be expanded to other situations than passing through stations at high speed, such as the interactions between a pair of high-speed trains fitted with these control devices passing each other in opposite directions, similar to the work of Huang et al. [24] on clean Maglev train models.

CRediT authorship contribution statement

Jordan Ashley Dunlop: Conceptualization, Methodology, Software, Validation, Formal analysis, Investigation, Data curation, Writing – original draft, Visualization,. **Mark Christopher Thompson:** Conceptualization, Methodology, Validation, Resources Writing – review & editing, Supervision, Project administration, Funding acquisition.

Declaration of competing interest

The authors declare that they have no known competing financial interests or personal relationships that could have appeared to influence the work reported in this paper.

Data availability

Data will be made available on request.

Appendix A. Preliminary testing results

Tables 7–9 provide the numerical data obtained from the preliminary series of analysis to allow for greater depth than presented in the body of the article, where this data is presented in Figs. 12–14.

This is particularly true of Table 7, where a drag deconstruction into the skin friction and pressure drag components is shown. This illustrates that particularly for the fin devices, the pressure drag is fluctuating significantly as the angle is varied.

The slipstream velocity measures are shown in Table 8. As in Fig. 13, this table shows that the *passenger side* of the parallel fins at large deflection angles were most successful at reducing the measure, although the thin front blockers also were capable of a significant reduction.

Table 9 provides the data which was presented in Fig. 14, illustrating the change in the mean downstream distance at which peak velocities were recorded. Again it is seen that the *passenger side* of the parallel fins at large deflection angles is where the location is altered significantly, with peaks recorded much further downstream.

Table 7
Summary of drag coefficients.

Case	ΔC_f (%)	ΔC_P (%)	C_D	ΔC_D (%)
Inwards fins				
2°	1.07	7.27	0.2872	4.75
3°	1.43	5.23	0.2843	3.70
4°	1.07	4.25	0.2823	2.95
5°	1.25	1.91	0.2787	1.65
6°	1.07	0.74	0.2766	0.89
7°	1.16	0.49	0.2763	0.78
Parallel fins				
2°	1.79	9.36	0.2914	6.28
3°	1.34	7.51	0.2879	5.01
4°	1.61	5.97	0.2857	4.20
5°	1.25	4.86	0.2835	3.41
6°	1.43	3.63	0.2817	2.75
7°	1.43	3.63	0.2817	2.75
Blocker plates				
Front	2.86	16.13	0.3036	10.74
Short front	1.52	9.24	0.2909	6.12
Thin front	2.95	10.59	0.2947	7.50
Full front	2.86	22.54	0.3140	14.54
Middle	3.31	11.95	0.2973	8.43
Thin middle	3.04	7.51	0.2898	5.69
Rear	−0.09	13.24	0.2956	7.82
Tall rear	0.36	30.17	0.3236	18.03
Thin rear	0.18	7.88	0.2872	4.77
Full rear	0.00	19.77	0.3063	11.74

Table 8
Summary of maximum velocity measures.

Case	Measure	% Change on baseline
Inwards fins		
2°	0.2946	11.94
3°	0.2909	10.53
4°	0.2905	10.39
5°	0.2655	0.87
6°	0.2551	−3.05
7°	0.2875	9.24
Parallel fins - Passenger side		
2°	0.2687	2.10
3°	0.2687	2.11
4°	0.2462	−6.46
5°	0.2517	−4.37
6°	0.2364	−10.16
7°	0.2314	−12.07
Parallel fins - Danger side		
2°	0.2784	5.80
3°	0.2691	2.26
4°	0.2579	−2.02
5°	0.2869	9.03
6°	0.2844	8.08
7°	0.2889	9.79
Blocker plates		
Front	0.2629	−0.12
Short front	0.2790	6.00
Thin front	0.2466	−6.30
Full front	0.2690	2.21
Middle	0.2695	2.41
Thin middle	0.2894	9.96
Rear	0.2759	4.84
Tall rear	0.2942	11.78
Thin rear	0.2656	0.92
Full rear	0.2742	4.20

Table 9
Summary of mean downstream distance.

Case	Mean downstream distance (L_{Ref} from tail)	% Change on baseline
Inwards fins		
2°	8.27	−12.70
3°	8.83	−6.88
4°	8.99	−5.18
5°	8.62	−9.07
6°	10.22	7.82
7°	9.21	−2.81
Parallel fins - Passenger side		
2°	9.61	1.42
3°	9.45	−0.30
4°	12.57	32.64
5°	12.21	28.87
6°	14.17	49.50
7°	14.43	52.32
Parallel fins - Danger side		
2°	10.27	8.33
3°	9.28	−2.05
4°	9.48	0.06
5°	9.63	1.67
6°	9.16	−3.31
7°	10.38	9.50

Table 9 (continued).

Case	Mean downstream distance (L_{Ref} from tail)	% Change on baseline
Blocker plates		
Front	9.53	0.58
Short front	8.69	−8.32
Thin front	9.87	4.16
Full front	9.04	−4.60
Middle	9.41	−0.65
Thin middle	9.20	−2.97
Rear	9.65	1.78
Tall rear	9.68	2.13
Thin rear	9.47	−0.09
Full rear	10.47	10.47

Table 10
Normalised mean maximum slipstream velocities for each of the five test lines.

Design case	Standard	Up	Down	In	Out
Baseline	0.1990	0.1670	0.2369	0.2296	0.1696
Inwards deflected fins	0.1959	0.1651	0.2316	0.2265	0.1679
Parallel fins - *Passenger Side*	0.1721	0.1596	0.1920	0.1871	0.1560
Parallel fins - *Danger Side*	0.1840	0.1513	0.2120	0.2111	0.1570
Thin front blocker plates	0.1941	0.1643	0.2257	0.2261	0.1626

Table 11
Percentage change in mean maximum slipstream velocities for each of the five test lines.

Design case	Standard	Up	Down	In	Out
Inwards deflected fins	−1.58	−1.19	−2.25	−1.34	−1.00
Parallel fins - *Passenger Side*	−13.54	−4.44	−18.95	−18.49	−8.03
Parallel fins - *Danger Side*	−7.56	−9.46	−10.54	−8.04	−7.45
Thin front blocker plates	−2.49	−1.67	−4.76	−1.50	−4.15

Table 12
Normalised slipstream velocity measure for each of the five test lines.

Design case	Standard	Up	Down	In	Out
Baseline	0.2849	0.2351	0.3309	0.3266	0.2409
Inwards deflected fins	0.2638	0.2309	0.3137	0.3032	0.2304
Parallel fins - *Passenger Side*	0.2284	0.2125	0.2577	0.2529	0.2036
Parallel fins - *Danger Side*	0.2819	0.2265	0.3194	0.3158	0.2425
Thin front blocker plates	0.2700	0.2289	0.3042	0.3099	0.2237

Table 13
Percentage change in maximum slipstream velocity measures for each of the five test lines.

Design case	Standard	Up	Down	In	Out
Inwards deflected fins	−7.41	−1.78	−5.20	−7.18	−4.36
Parallel fins - *Passenger Side*	−19.84	−9.61	−22.12	−22.57	−15.50
Parallel fins - *Danger Side*	−1.06	−3.64	−3.45	−3.32	0.65
Thin front blocker plates	−5.25	−2.63	−8.06	−5.11	−7.13

Table 14
Mean downstream distance of maximum slipstream velocities for each of the five test lines, in units of L_{Ref} from rear of model.

Design case	Standard	Up	Down	In	Out
Baseline	10.17	13.25	8.31	8.35	13.10
Inwards deflected fins	10.17	12.82	8.62	7.83	12.76
Parallel fins - *Passenger Side*	15.80	18.11	12.49	13.27	19.49
Parallel fins - *Danger Side*	9.74	12.02	10.10	8.78	12.97
Thin front blocker plates	10.45	12.99	8.58	7.77	12.85

Appendix B. Secondary testing results

Tables 10 and 12 provide the slipstream velocity data shown in Fig. 16, while Tables 11 and 13 show the percentage variation in comparison to the baseline values. These provide extra detail to supplement Fig. 16.

Table 14 provides the values of mean downstream distance that are summarised as percentage variations on the baseline in Table 6.

References

[1] J.R. Bell, D. Burton, M.C. Thompson, A.H. Herbst, J. Sheridan, Wind tunnel analysis of the slipstream and wake of a high-speed train, J. Wind Eng. Ind. Aerodyn. 134 (2014) 122–138.

[2] C. Baker, M. Sterling, G. Figura-Handy, T. Johnson, P. Free, G. Munley, I. Bowman, C. Pope, R. Gawthorpe, The Effect of Train Slipstreams on Passengers and Trackside Workers, Technical Report, Rail Safety and Standards Board Ltd, 2006.

[3] C. Baker, A. Quinn, M. Sima, L. Hoefener, R. Licciardello, Full-scale measurement and analysis of train slipstreams and wakes. Part 1: Ensemble averages, J. Rail Rapid Transit. 228 (2014) 451–467.

[4] C. Baker, A. Quinn, M. Sima, L. Hoefener, R. Licciardello, Full-scale measurement and analysis of train slipstreams and wakes. Part 2: Gust analysis, J. Rail Rapid Transit. 228 (2014) 468–480.

[5] D. Liu, G.M. Tomasini, D. Rocchi, F. Cheli, Z. Lu, M. Zhong, Correlation of car-body vibration and train overturning under strong wind conditions, J. Mech. Syst. Signal Process. 142 (2020).

[6] J.R. Bell, D. Burton, M.C. Thompson, A.H. Herbst, J. Sheridan, Flow topology and unsteady features of the wake of a generic high-speed train, J. Fluids Struct. 61 (2015) 168–183.

[7] J.R. Bell, D. Burton, M.C. Thompson, A.H. Herbst, J. Sheridan, Dynamics of trailing vortices in the wake of a generic high-speed train, J. Fluids Struct. 65 (2016) 238–256.

[8] J.R. Bell, D. Burton, M.C. Thompson, A.H. Herbst, J. Sheridan, The effect of tail geometry on the slipstream and unsteady wake structure of high-speed trains, Exp. Therm Fluid Sci. 83 (2017) 215–230.

[9] J.R. Bell, D. Burton, M.C. Thompson, A.H. Herbst, J. Sheridan, Moving model analysis of the slipstream and wake of a high-speed train, J. Wind Eng. Ind. Aerodyn. 136 (2015) 127–137.

[10] N. Gil, C. Baker, C. Roberts, The measurement of train slipstream characteristics using a rotating rail rig, in: BBAA VI International Colloquium on Bluff Bodies Aerodynamics & Applications, 2008.

[11] H. Hemida, C. Baker, The calculation of train slipstreams using Large-Eddy Simulation techniques, in: 9th World Congress on Railway Research, Lille, May 22-26, 2011.

[12] T.W. Muld, Slipstream and Flow Structures in the near Wake of High-Speed Trains, Technical Report, Royal Institute of Technology, Sweden, 2012.

[13] G. Chen, X. Li, Z. Liu, D. Zhou, Z. Wang, X. Liang, S. Krajnovic, Dynamic analysis of the effect of nose length on train aerodynamic performance, J. Wind Eng. Ind. Aerodyn. 184 (2019) 198–208.

[14] R. Li, P. Xu, S. Yao, Optimization of the high-speed train head using the radial basis function morphing method, Inst. Mech. Eng. 234 (2020) 96–107.

[15] J. Wang, G. Minelli, T. Dong, G. Chen, S. Krajnovic, The effect of bogie fairings on the slipstream and wake flow of a high-speed train. An IDDES study, J. Wind Eng. Ind. Aerodyn. 191 (2019) 183–202.

[16] T. Dong, G. Minelli, J. Wang, X. Liang, S. Krajnovic, The effect of ground clearance on the aerodynamics of a generic high-speed train, J. Fluids Struct. 95 (2020).

[17] S. Wang, J.R. Bell, D. Burton, A.H. Herbst, J. Sheridan, M.C. Thompson, The performance of different turbulence models (URANS, SAS and DES) for predicting high-speed train slipstream, J. Wind Eng. Ind. Aerodyn. 165 (2017) 46–57.

[18] S. Wang, D. Burton, A. Herbst, J. Sheridan, M.C. Thompson, The effect of the ground condition on high-speed train slipstream, J. Wind Eng. Ind. Aerodyn. 172 (2018) 230–243.

[19] C. Baker, The flow around high speed trains, J. Wind Eng. Ind. Aerodyn. 98 (2010).

[20] B. Shulte-Werning, C. Heine, G. Matschke, Unsteady wake flow characteristics of high-speed trains, in: Proceedins in Applied Mathematics and Mechanics, 2003.

[21] J. Dunlop, Slipstream Control for High-Speed Trains (Ph.D. thesis), Monash University, 2021.

[22] J.N. Kutz, S.L. Brunton, B. Brunton, J.L. Proctor, Dynamic mode decomposition, 2016, chapter 2.

[23] L. Sirovich, Turbulence and the dynamics of coherent structures Part i: Coherent structures, Quart. Appl. Math. 45 (3) (1987) 561–590.

[24] S. Huang, Z. Li, M. Yang, Aerodynamics of high-speed maglev trains passing each other in open air, J. Wind Eng. Ind. Aerodyn. 188 (2019) 151–160.